# UNIVERSITÀ DEGLI STUDI DI PADOVA

Dipartimento di Fisica e Astronomia "Galileo Galilei"

Master Degree in Physics

Final Dissertation

## Study of DNA damage by beta radiation using Geant4-DNA in the context of the ISOLPHARM project

Thesis supervisor

Prof. Marcello Lunardon

Thesis co-supervisor

Dr. Alberto Arzenton

Dr. Alberto Andrighetto

Candidate

Aurora Leso

Academic Year 2022/2023

*All'Aurora del passato,*
*alle sue paure e incertezze.*
*All'Aurora del futuro,*
*alle sue vittorie e conquiste.*

# Abstract

This thesis is part of the ISOLPHARM project, which aims to produce high-purity radioisotopes for use in diagnostic and therapeutic nuclear medicine applications by utilizing the second-generation ISOL facility SPES (Selective Production of Exotic Species) at INFN-LNL. The focus of this thesis is to investigate the potential DNA damage caused by radiation from two radioisotopic sources, $^{111}$Ag and $^{60}$Co, using the GEANT4-DNA simulation toolkit, an extension of the GEANT4 software. The results are fundamental for the ADMIRAL experiment, which aims to evaluate the diagnostic and therapeutic power of radiopharmaceuticals containing the innovative radionuclide $^{111}$Ag. Currently, the radiobiological analysis of radiopharmaceuticals is not extensively investigated as the external irradiation experiments due to the complexity of defining and studying the absorbed dose in a cell culture irradiated by an internalized radiopharmaceutical. To overcome this, the thesis proposes the usage of the MIRD schema to compute the damage rate in the form of S-values. These values can be associated with biophysical models to predict experimental results such as *foci* assays and cell survival. In particular, the *foci* technique can provide a direct measurement of the extent and distribution of DNA damage induced by ionizing radiation, so that it can be used as an experimental test to verify the validity of GEANT4-DNA simulation results.

# Contents

# Part I

# Background and Context

# Chapter 1

# Introduction

In this chapter we shortly recall some preliminary notions useful to introduce the following topics. Specifically, the focus will be placed on **radiobiology** and **dosimetry** notions.

## 1.1 Radiobiology notions

The purpose of this section is to explain in a clear and concise way how ionizing radiation can harm cells.

**Radiation interactions with matter** When a cell is exposed to ionizing radiation, the energy from the radiation generates a large number of highly reactive molecules inside it, such as free radicals and reactive oxygen species (i.e. hydroxyl groups and peroxides). These molecules are difficult for the cell to remove and can disrupt its normal functions.

If the radiation damages the DNA in the nucleus, the situation becomes even more severe: as a matter of fact, cells can normally repair damage to one strand of the DNA by using the information contained in the complementary strand. However, a high concentration of free radicals can interfere with this process, making it more difficult for the cell to repair the damage. Moreover, if both DNA strands are damaged in the same location, repairing the damage becomes almost impossible, and can lead to chromosomal aberrations that are generally lethal to the cell during the division stage, due to the fact that daughter cells will be receiving an incorrect number or structure of chromosomes.

Specifically, ionizing radiation can have both deterministic and stochastic effects: deterministic effects refer to cell death, which occurs when a particular threshold of absorbed dose is overcome, while stochastic effects happen randomly and without a threshold. The last ones are of greater concern from a medical and radioprotection perspective, since they can lead to serious illnesses such as cancer, cataracts, and heritable diseases.
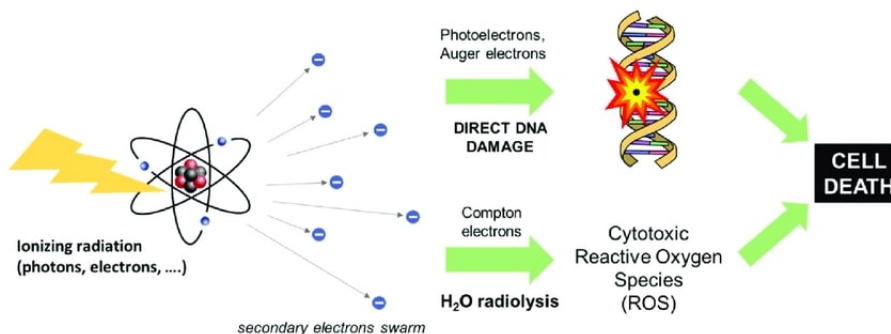


Figure 1.1: Scheme of the interaction of the incident ionizing radiation with matter: secondary charges can induce cellular death by (i) directly damaging their DNA or (ii) by enhancing the water radiolysis reaction that produces highly cytotoxic reactive oxygen species. Image from [1]

Obviously, the incidence of these illnesses increases in proportion to the absorbed dose of radiation, depending on the mass, charge and energy of radiation. High-energy radiation, such as gamma rays and X-rays, has a high penetration power and can pass through thick layers of materials, including the human body. Consequently, they can damage cells and tissues throughout the body. In contrast, alpha particles, heavier and charged, have a shorter range in matter and are easily absorbed by the first few layers of atoms in a material, such as skin or clothing. Therefore, they are not generally a significant external radiation hazard, as they cannot penetrate deeply into the body or pass through most materials. However, if alpha-emitting radioactive materials are ingested or inhaled, they can be a significant internal radiation hazard. When alpha particles are emitted within the body, they deposit their energy over a very short distance, causing significant damage to nearby cells and tissues. [2]

**DNA damage and repair mechanisms**      DNA damage caused by ionizing radiation can have significant consequences for the affected cells and tissues. When ionizing radiation interacts with DNA, it can cause a variety of different types of damage, including single-strand breaks, double-strand breaks, base damage, and cross-linking.
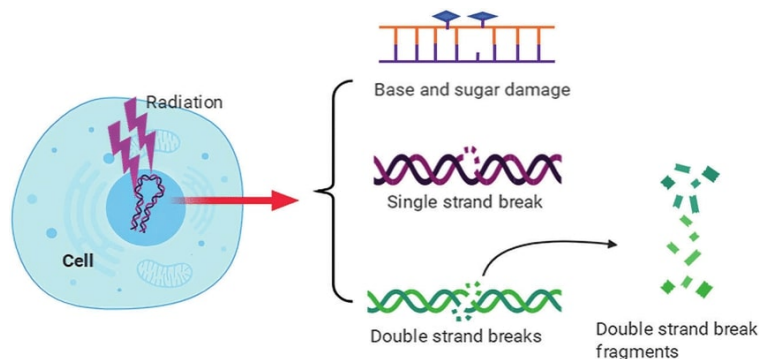


Figure 1.2: Schematic of the types of DNA damage, ranging from single and clustered damage sites through to simple and complex DSBs, formed by passage of a single radiation track. Image from [3]

Single-strand breaks (SSBs) occur when one of the two strands of the DNA molecule is broken, and this damages can be repaired by a mechanism called base excision repair. In this process, specialized enzymes recognize the damaged nucleotide and remove it from the DNA strand. The gap is then filled by DNA polymerase, and the DNA ligase seals the remaining discontinuity.

Double-strand breaks (DSBs), on the other hand, are much more severe and can be difficult for the cells to repair. When both strands of the DNA molecule are broken at the same location, the cell's repair mechanisms may struggle to restore the original structure of the DNA molecule.

Cells have two primary pathways for repairing double-strand breaks: non-homologous end joining (NHEJ) and homologous recombination (HR). NHEJ is the most common pathway for repairing double-strand breaks and involves the direct ligation of the broken ends of the DNA molecule. This process can lead to the loss of some genetic information at the site of the break. HR, on the other hand, is a more complex process that involves the use of the undamaged sister chromatid as a template to repair the break. This process is more accurate and does not result in the loss of genetic information.

In higher eukaryotes, such as humans, there are several primary pathways available to repair DSBs. These pathways include non-homologous end-joining (NHEJ), homologous recombination (HR), single-strand annealing (SSA), and at least two alternative end-joining mechanisms. NHEJ, SSA, and alternative end-joining pathways are considered error-prone because they can introduce mutations during the repair process, while HR is generally regarded as error-free. The repair pathway choice depends on the specific stage of the cell cycle. In mammalian and human cells, NHEJ is the primary mechanism for repairing DSBs throughout all phases, since this pathway does not require a homologous DNA template and is, therefore, more common. On the other hand, HR is restricted to the late S and G2 phases since it relies on a sister chromatid or a similar undamaged DNA sequence as a template for accurate repair. During the mentioned cell cycle phases, the cell has replicated its DNA, and a sister

chromatid is present as an identical copy that can be used as a template for HR-mediated repair. This allows HR to perform more precise and error-free repair by using the intact DNA sequence as a reference to re-build the damaged one. A specialized form of HR that is worth mentioning is HR-h. This mechanism involves the exchange of genetic information between non-identical or heterozygous DNA sequences, and is crucial for repairing DSBs specifically during meiosis. HR-h relies on the same end-resection mechanism as HR and requires the presence of a homologous DNA template for repair. SSA is a homology-directed DNA repair pathway that promotes recombination between repeated DNA sequences: this means that it operates similarly to HR but requires a distinct set of proteins.
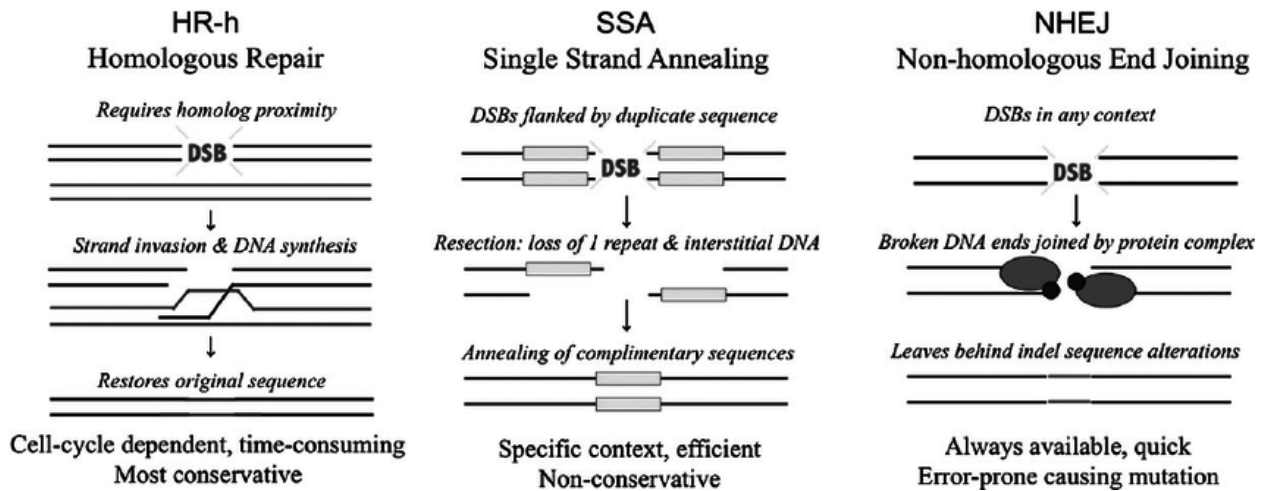


Figure 1.3: Comparison of the alternative DSB repair pathways. HR-h (Homologous Recombination-High) refers to a more accurate and high-fidelity mode of HR repair. Image from [4]

As introduced before, in addition to NHEJ, SSA, and HR, there are two alternative end-joining pathways commonly applied by cells: microhomology-mediated end-joining (MMEJ) and Alt-NHEJ. MMEJ, similarly to SSA, relies on pre-existing microhomologies, which are short regions of sequence similarity located in the surroundings of the DSB site. These microhomologies, typically a few base pairs in length, are used as points of alignment and annealing between the broken DNA ends. Once they are aligned, the DNA sequences between them (DSB site included) are removed or excised, so that the remaining ends can be ligated together to complete the repair process.

On the other hand, Alt-NHEJ does not require pre-existing microhomologies to perform the repair. Instead, it relies on the activity of a protein called poly ADP-ribose polymerase (PARP) to mediate the repair process. PARP plays a role in recruiting and activating repair factors that can process and join the DNA ends in a more flexible manner, even in the absence of microhomologies. Alt-NHEJ can be error-prone, resulting in potential DNA rearrangements or deletions at the repair site. [5]

Base damage occurs when the ionizing radiation interacts with one of the four nitrogenous bases that make up the DNA molecule, causing it to become chemically altered. This type of damage can lead to mutations in the DNA sequence, which can potentially affect the function of the affected gene. Cross-linking occurs when the ionizing radiation causes two adjacent nucleotides in the DNA molecule to become chemically bonded. This type of damage can prevent the DNA from being replicated and transcribed correctly, which can lead to cell death or genetic mutations. The ability of cells to repair DNA damage caused by ionizing radiation depends on a variety of factors, including the type, energy, and dose of the radiation. Understanding the nature of DNA damage caused by ionizing radiation and the mechanisms that cells use to repair this damage is essential for developing effective strategies to protect individuals from the harmful effects of ionizing radiation. [4, 6]

## 1.2 The MIRD schema

This paragraph recalls some basic concepts related to the MIRD schema.

**Mean Absorbed Dose Rate**  The absorbed dose D is defined as

$$D = \frac{dE}{dm} \tag{1.1}$$

where dE is the mean energy imparted by ionizing radiation to matter of mass dm.
The unit of the absorbed dose is the joule per kilogram (J kg$^{-1}$), given the special name gray (Gy):

$$1 \text{ Gy} = \frac{1 \text{ J}}{1 \text{ kg}} \tag{1.2}$$

The time-dependent rate at which the absorbed dose is delivered $\dot{D}(r_T, t)$ to target tissue $r_T$ within a patient from a radioactive material distributed uniformly within source tissue $r_S$ at time t after administration is given as:

$$\dot{D}(r_T, t) = \sum_{r_S} A(r_S, t) S(r_T \leftarrow r_S, t) \tag{1.3}$$

where $A(r_S, t)$ is the time-dependent activity of the radiopharmaceutical in $r_S$ and $S(r_T \leftarrow r_S, t)$ is the radionuclide-specific quantity representing the mean absorbed dose rate to $r_T$ at time t after administration per unit activity present in $r_S$. We can even define a time-dependent equation for the mean absorbed dose, which is

$$D(r_T, T_D) = \int_0^{T_D} \dot{D}(r_T) dt = \sum_{r_S} \int_0^{T_D} A(r_S, t) S(r_T \leftarrow r_S, t) dt \tag{1.4}$$

**S-values**  The quantity S is specific to the radionuclide and to the computational phantom defining the spatial relationship and tissue compositions of $r_S$ and $r_T$ and their intervening tissues in the reference individual or tissue model. S is given as:

$$S(r_T \leftarrow r_S, t) = \frac{1}{M(r_T, t)} \sum_i E_i Y_i \phi(r_T \leftarrow r_S, E_i, t) \tag{1.5}$$

where $E_i$ is the mean (or individual) energy of the i$^{\text{th}}$ nuclear transition, $Y_i$ is the number of i$^{\text{th}}$ nuclear transitions per nuclear transformation, $\phi(r_T \leftarrow r_S, E_i, t)$ is the absorbed fraction (defined as the fraction of radiation energy $E_i$ emitted within $r_S$ at time t that is absorbed in $r_T$) and $M(r_T, t)$ is the time-dependent mass of the target tissue $r_T$ in the reference individual. Since the time dependency of S can generally be neglected, as when the source and target masses remain constant over the period of irradiation, 1.4 may be reduced to the following time-independent form:

$$D(r_T, T_D) = \sum_{r_S} \tilde{A}(r_S, T_D) S(r_T \leftarrow r_S) \tag{1.6}$$

where

$$\tilde{A}(r_S, T_D) = \int_0^{T_D} A(r_S, t) dt \tag{1.7}$$

is the time integrated activity. [7–9]

This schema, proposed by the Committee on Medical Internal Radiation Dose (MIRD) of the American Society of Nuclear Medicine and Molecular Imaging (SNMMI), is a widely used method for performing dosimetry calculations in nuclear medicine and radiation therapy. It was first developed in the 1960s to provide a standardized framework for estimating the radiation dose to organs and tissues from internalized radioactive sources. The MIRD schema takes into account various factors that can affect the radiation dose, such as the physical characteristics of the radiation source, the

route of administration, and the biological distribution of the radioactive material. It also includes models for calculating the absorbed dose in different types of tissues, such as bone, soft tissue, and red marrow. The strategy applied to associate the computed damage S-values, which are calculated using the MIRD schema, with an appropriate biophysical model and predicting experimental results consists of four main steps:

- The creation of a virtual volume made of a given material or tissue, subdivided in elementary units such as concentric shells or voxels (in GEANT4, they can be classified as sensitive volumes in order to count the deposited energy);

- The collocation of a radiation source inside the volume, paying attention to its symmetries;

- The Monte Carlo simulation of a high number of time-independent radiation events, followed by the calculation of the mean absorbed dose per event in every shell (Dose Point Kernel, DPK) or voxel (Voxel S-Value, VSV). In particular, DPK calculates the absorbed dose in the target organ or tissue by representing the mean absorbed dose per event in every shell of the virtual volume, while VSV estimates the radiation absorbed dose in a specific voxel of the virtual volume by representing the mean absorbed dose per event in that voxel.

- The convolution between the obtained kernel and a function expressing the activity distribution in the sample, for example a PET or SPECT 3D image.

By following these four main steps, it is possible to calculate the absorbed dose of radiation in a target tissue or organ, taking into account various factors that can affect the radiation dose. This information can be used to optimize radiation therapy and improve patient outcomes. [10]
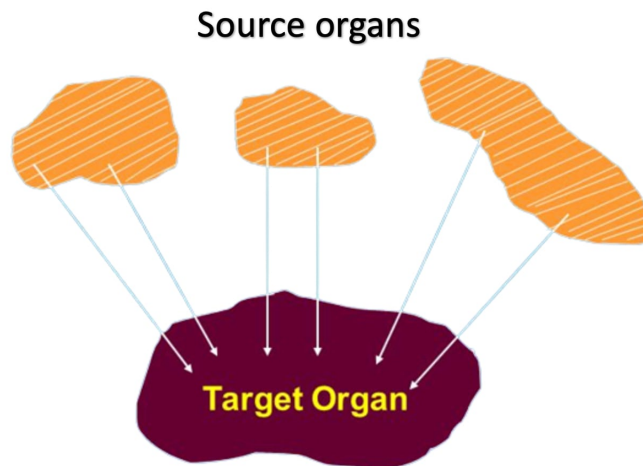


Figure 1.4: Concept of the MIRD schema. Every target organ can be a source organ too.

# Chapter 2

# The ISOLPHARM project

The thesis' work is part of the ISOLPHARM (ISOL technique for radioPHARMaceuticals) project headed by the Legnaro National Laboratory (LNL) of the Italian Institute for Nuclear Physics (INFN). Born in 2017, ISOLPHARM is a pioneering initiative that aims to produce high-purity radioisotopes for use in both diagnostic and therapeutic nuclear medicine applications. It has the main purpose of utilizing the second-generation ISOL facility SPES (Selective Production of Exotic Species) in order to obtain highly pure innovative radionuclides that have medical relevance. In addition to INFN, several other institutions are participating in the experiments, including the University of Padova. Specifically, the Department of Physics and Astronomy "Galileo Galilei", the Department of Chemistry, and the Department of Pharmaceutical and Pharmacological Sciences are all involved in the research.



Figure 2.1: The ISOLPHARM logo.

To date, there have been three pilot experiments conducted in the ISOLPHARM project:

1. **ISOLPHARM_Ag** (2018-2019): investigate the production and release capabilities of $^{111}$Ag from the SPES fission target and study the feasibility of purification techniques for Ag$^+$ and possible targeting agents to transport $^{111}$Ag to specific tumor cells [11].

2. **ISOLPHARM-EIRA** (2020-2022): the research was divided in three main tasks (see Fig. 2.2):
   - Task 1, physics: production of $^{111}$Ag with the TRIGA MARK II reactor at the Laboratory of Applied Nuclear Energy (L.E.N.A.) in Pavia by activation of a $^{110}$Pd enriched target [12, 13]; the resonant laser ionization (RLI) technique was tested to improve the ionization and extraction of $^{111}$Ag from the SPES primary target [14, 15]

   - Task 2, chemistry: synthesis and characterization of first prototype molecules for chelators, linkers, targeting agents, and development of radioisotope purification [16–18];

   - Task 3, biology: selection of *in vitro* models to evaluate the best radiopharmaceutical precursor for preliminary *in vivo* studies [19].
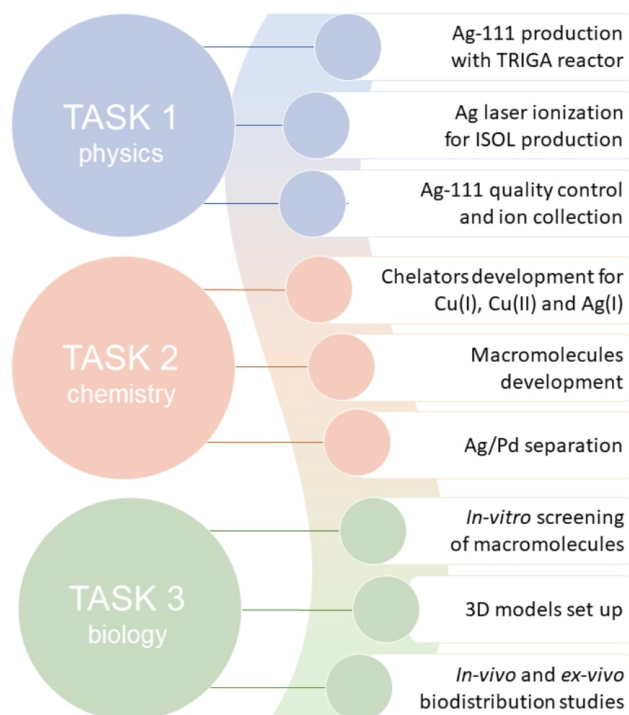
Figure 2.2: Representation of the ISOLPHARM_EIRA main objectives, divided into Tasks [20].

3. **ADMIRAL** (2023-2025): evaluation of the diagnostic and therapeutic power of radiopharmaceuticals containing the innovative radionuclide $^{111}$Ag [21].

The four main work packages of the ADMIRAL experiment, in which the thesis' work locates, follow:

- **WP1, radiopharmaceutical production**: optimize the radioisotopic production and purification of $^{111}$Ag via traditional methods since the ISOL technique is not available. Due to the ongoing SPES construction, the TRIGA Mark II nuclear reactor at L.E.N.A. (Fig. 2.3) will be involved in $^{111}$Ag production. This involves conducting radiochemistry experiments focused on the dissolution of the irradiated target to obtain $^{111}$Ag and finding ways to insert the radionuclides into a macromolecular context that can effectively bind and transport them to tumor tissues, specifically targeting cancer cells.



Figure 2.3: The TRIGA MARK II nuclear reactor at L.E.N.A. [21] .

- **WP2, $\beta$-imaging**: design, construct, and characterize a device that utilizes monolithic silicon pixel technology (ALPIDE chips, see Fig. 2.4) to capture high-resolution "$\beta$-pictures" of 2D

cellular cultures or thin 3D slices (scaffolds) containing $\beta$-emitters.



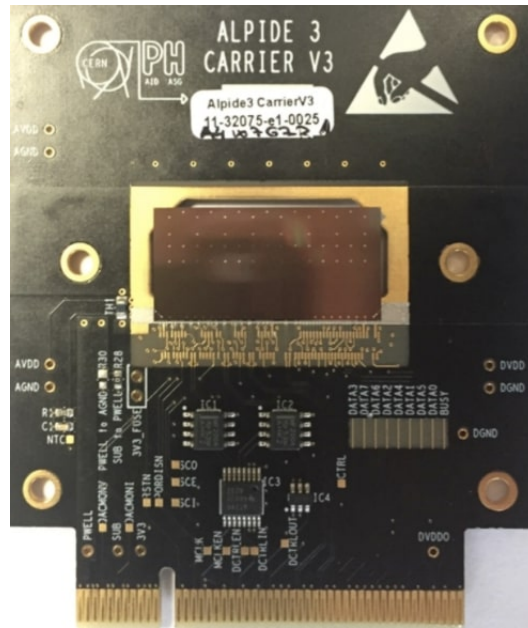Figure 2.4: Example of ALPIDE chip [21].

- **WP3, $\gamma$-imaging**: design and characterize a $\gamma$-camera for detecting $\gamma$ radiation emitted during the decay of $^{111}$Ag (see Fig. 2.5). The aim is to optimize the coupling between scintillators and silicon photomultipliers (SiPMs) and develop suitable electronics and data acquisition systems (DAQs) with the final goal to realize a basic module of a SPECT device optimized for $^{111}$Ag. The acquired knowledge will be used to build a planar system for the detection of $^{111}$Ag. The results will be compared with existing preclinical devices designed for other medical nuclides and with the Bruker In-Vivo Xtreme II system available in Trento or Catania.
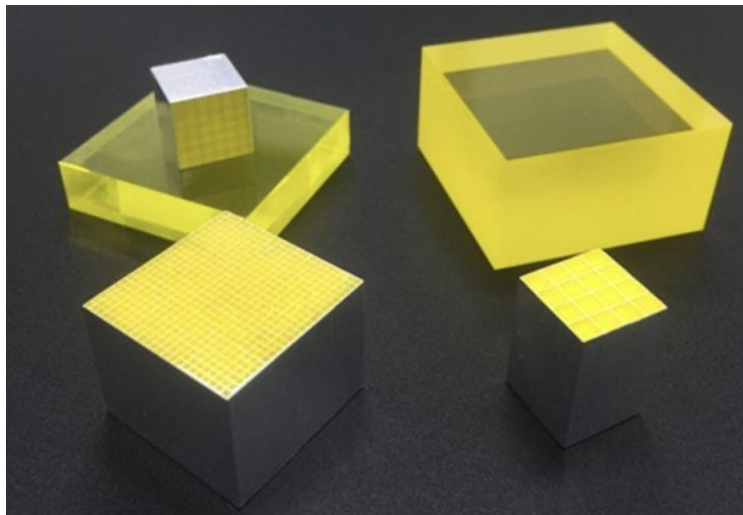


Figure 2.5: Simulation of $\gamma$ camera [21].

- **WP4, targeted radiobiology**: study the effects of $^{111}$Ag targeted radionuclide therapy (TRT) on cell survival using a "targeted" radiobiology approach. In particular, a tumoral cell line overexpressing CCK2R (cholecystokinin 2 receptor) will be selected and grown in T75 flasks at the biology laboratories of Pavia University (see schematic procedure in Fig. 2.6). The effects of $^{111}$Ag TRT on both 2D cell and 3D cell cultures obtained through bioprinting will be analyzed. Finally, the radiobiological data are going to be correlated with the absorbed dose at the cellular level, computed using the Monte Carlo method.[21]

11

Figure 2.6: Representation of the main steps of cell survival experiment [21].

## 2.1 The ISOL technique

The ISOL (Isotope Separation On-Line) method, as mentioned before, is a technique used for producing specific radionuclides. In this approach, a proton beam is accelerated by a cyclotron and directed towards a solid target, leading to the the production of a series of exotic nuclei via nuclear reactions that depend both on the target composition and on the proton energy. The primary target material for ISOLPHARM is a fissile target composed of seven disks, with diameter 40 mm and thickness 0.8 mm, made of uranium carbide, a composite material comprising uranium dicarbide ($UC_2$), graphite (C), and a lower concentration of uranium monocarbide (UC). After the production of nuclides, they disperse throughout the target. Thanks to the high temperature of 2000°C maintained in the system, the volatile elements are evaporated and effused through a transfer line. The effused elements are then led into an ionizing high vacuum chamber that maintains a pressure of about $10^{-6}$ to $10^{-5}$ mbar, where they are ionized to a +1 charge state, in order to be extracted and accelerated using a high voltage of up to 40 kV, generating the Radioactive Ion Beams (RIBs). Each element is assigned a coefficient $\epsilon$, which represents the product of the contributions in efficiency for each stage. While not every nuclide is able to reach the accelerator due to the varying efficiency of each stage, the use of coefficients $\epsilon$ helps to account for these differences. The resulting RIB, containing only the nuclide of interest and its isobars, is deposited into a collection target.

In the context of ISOLPHARM, the pure radionuclide obtained as described is then bound to a carrier molecule to create the radiolabeled drug. This molecule consists of three main components:

- **Chelator**: binds the radionuclide stably with coordination covalent bonds;

- **Targeting agent**: takes the radionuclide to the cancer cells that interact with specific receptors overexpressed in their plasma membrane;

- **Linker** (or spacer): connects the chelator and the targeting agent preventing interactions between them.
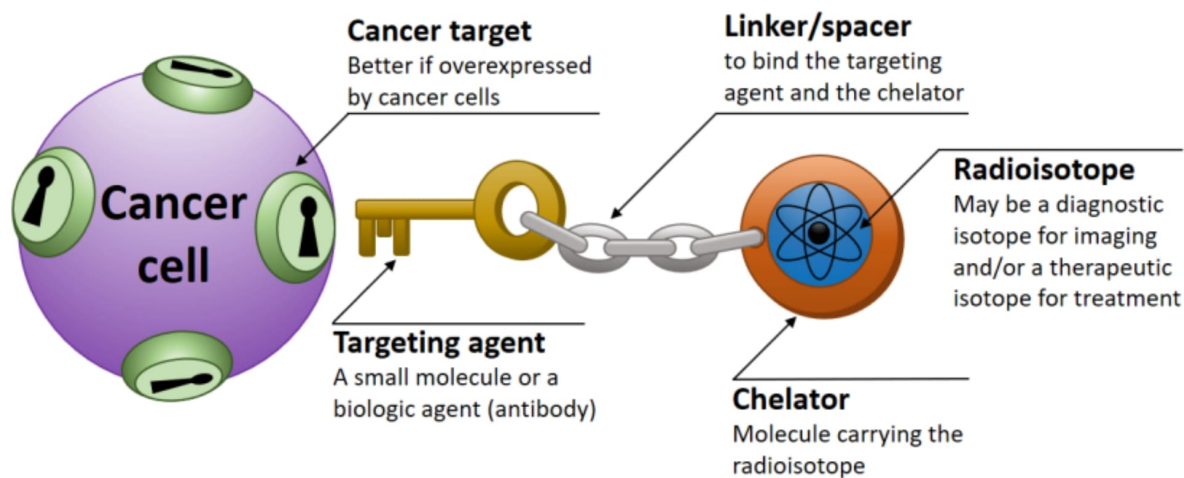
The scheme is shown in Fig. 2.7:



Figure 2.7: Mechanism of targeting and structural segmentation of a carrier molecule for radiopharmaceuticals.

Before being commercialized, radiopharmaceuticals undergo a series of *in vitro* and *in vivo* experiments to test their ability to distribute correctly in the affected tissues, deliver an appropriate dose of radiation to the targeted site, and minimize damage to healthy organs. Once these tests are successfully completed, the radiopharmaceuticals can enter the clinical sperimentation. The whole production process is depicted in Fig. 2.8.[11, 12, 22]
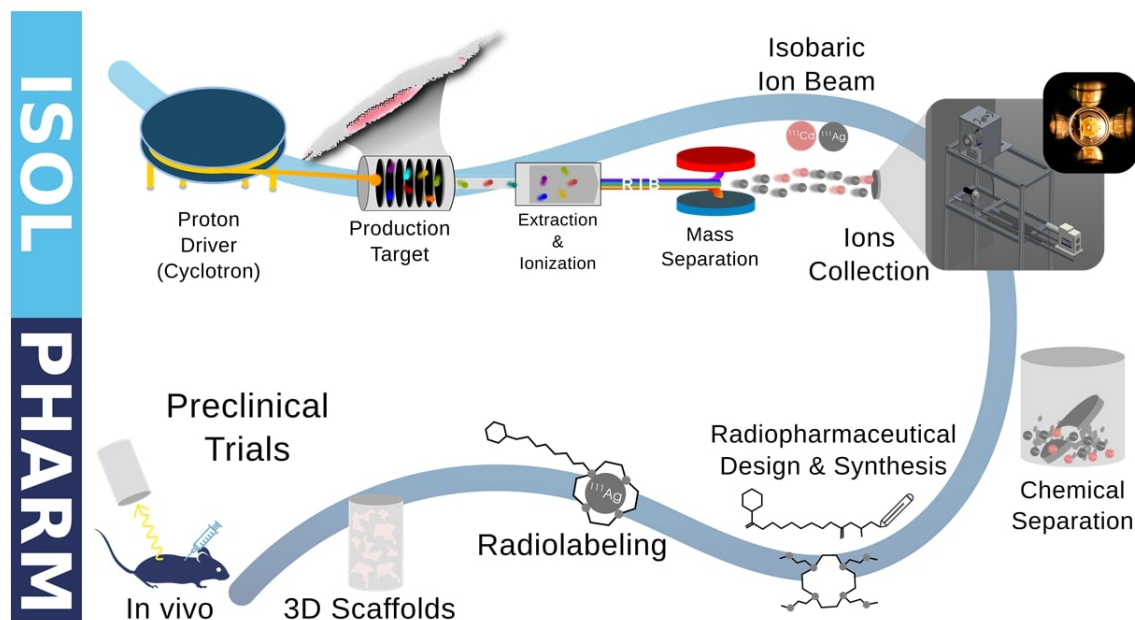


Figure 2.8: Depiction of the entire radiopharmaceutical production process for ISOLPHARM.

Concerning the radionuclide, the following characteristics have to be considered when choosing a particular species for nuclear medicine applications:

- **Half-Life**: it should be comprised between a few hours and some days to facilitate the essential logistical steps such as separation from the target, radiolabeling procedures and distribution to medical facilities;

- **Toxicity**: it should be the lowest possible, in order to minimize the impact of ionizing radiation on healthy tissues. This factor is influenced by both physical attributes (i.e., half-life, type of emitted radiation) and physiological characteristics (i.e., absorption within the body, deposition sites, elimination rates);

- **Chemical properties**: the radionuclide has to exhibit suitable chemical properties that enable efficient target separation and successful radiolabeling techniques;

- **Costs of production**: the entire radiopharmaceutical supply chain, comprehending the production, the radiochemical processing and the distribution, must be economically sustainable.

Other two fundamental quality criteria that are typically taken into account when assessing the quality of a produced radionuclide are:

- **Radionuclidic purity**: is defined as "the ratio, expressed as a percentage, of the radioactivity of the desired radionuclide to the total radioactivity of the source". This quantity holds significant importance in radiopharmacy because the presence of any impurities may increase the radiation dose recieved by the patient and can also compromise the quality of any imaging procedures conducted [23];

- **Specific activity**: it is the ratio between the compound activity and its mass. This parameter is fundamental in the quantification of the amount of cold isotopes that can be present in the preparation. The challenge with non-radioactive isotopes is based on the fact that the therapeutic efficacy lowers as the limited number of receptors on the cell surface (refer to Fig. 2.9) occupied by non-radioactive isotopes increases.
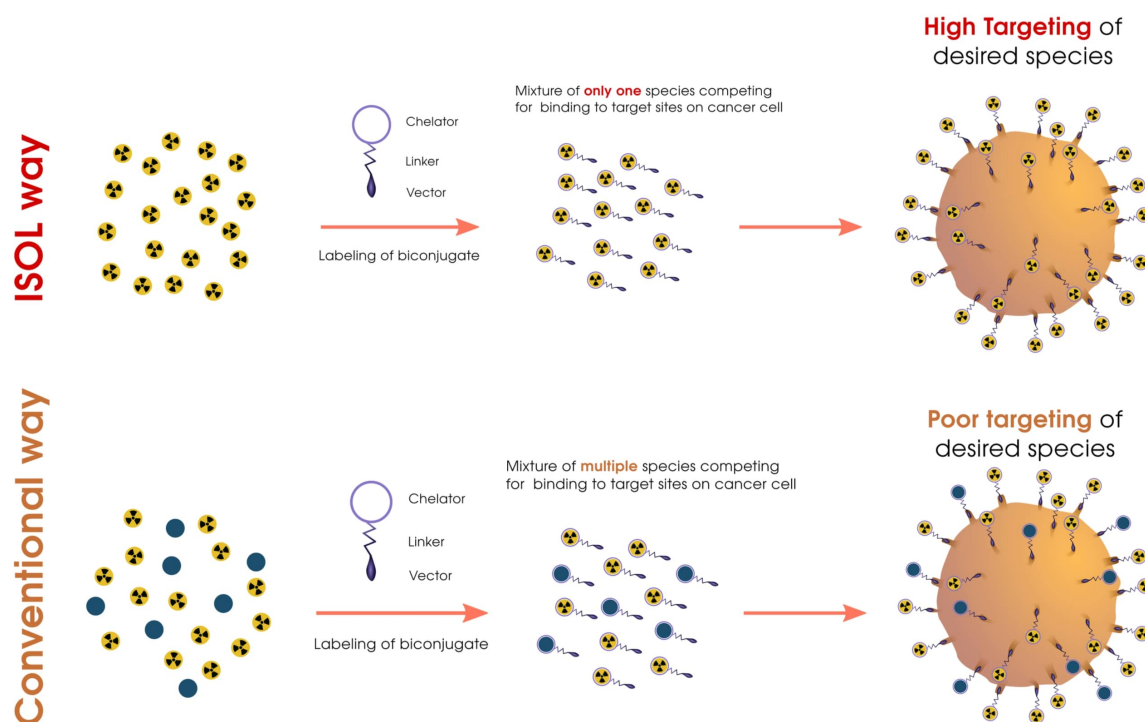


Figure 2.9: Difference between Carrier-Added and Carrier-Free Radiopharmaceuticals [24].

## 2.2 The innovative radionuclide $^{111}$Ag

The unique nuclear properties of $^{111}$Ag make it an attractive radionuclide for various applications in nuclear medicine. As an isotope of silver (Z = 47) with 64 neutrons (N = 64), $^{111}$Ag has a half-life $t_{\frac{1}{2}}$ = 7.45 days that is well-suited for both diagnostic imaging and targeted radionuclide therapy, since it is long enough to allow for the synthesis and distribution of radiopharmaceuticals, yet short enough to minimize patient radiation exposure.

In addition to its favorable half-life, even the $\beta^-$ emission of $^{111}$Ag is another essential feature: the decay of $^{111}$Ag to the stable isobar $^{111}$Cd is highly favorable due to its release of an energy (mean energy of 360.4 keV in 92% of cases and 223.5 keV in 7.1%, with an endpoint at 1.0368 MeV) that is well-suited for therapeutic purposes, as it can penetrate tumor tissue and deliver a high dose of radiation to cancerous cells while minimizing damage to surrounding healthy tissue. The beta emission of $^{111}$Ag also enables its use in imaging applications. The gamma ray emissions of the radionuclide at 245.40 keV and 342.13 keV are ideal for imaging using conventional gamma cameras and single-photon emission computed tomography (SPECT) imaging. This allows for the non-invasive visualization of physiological processes *in vivo*, such as blood flow and metabolism, as well as the detection of cancer and other diseases. [11, 22, 25–27]

## 2.3 CloudVeneto

The high computational resources requested by the simulation, due to the complex geometries and interactions being modeled, exceeded the capabilities of a laptop. To address this challenge, it was decided to use CloudVeneto (logo in Fig. 2.10), a cloud computing platform.



Figure 2.10: Cloudveneto logo.

CloudVeneto brings together ten departments from the University of Padova, the Padova Section of INFN (National Institute of Nuclear Physics), and the Legnaro National Laboratories of INFN in a collaborative effort. These entities offer to users an easy access to a cutting-edge Cloud-based infrastructure. Moreover, the INFN resources within CloudVeneto are integrated with the broader national INFN Cloud framework.

This platform, resting on the use of OpenStack Cloud middleware, is a IaaS (Infrastructure as a Service) Cloud service, since it efficiently manages a pool of computing resources that can be swiftly and effectively allocated to users upon request. In practical terms, users can easily ask for and configure even intricate computing systems tailored to their specific needs. CloudVeneto is particularly useful in scenarios requiring scalability since, in such cases, having substantial computing resources is fundamental to strongly reduce the time it takes for a process to run.

In the thesis' work, this service was fundamental to allow the run of the longest simulations, namely the ones with human cell geometry and the highest number of events.

## 2.4 Thesis motivation

The radiobiological analysis of radiopharmaceuticals is still less represented in literature compared to the same kind of experiments using external irradiation, mainly because defining and studying the absorbed dose in a cell culture irradiated by an internalized radiopharmaceutical is quite complex compared to the same situation but with an external irradiating source. As a matter of fact, with respect to external beam radiotherapy

- The dose-rate per cell depends on the amount of cell receptors and consequently on the number of cells in the culture at a given time $t$;
- Radiation decays in time and is not administered in uniform cycles;
- The exposure time is expected to be comparable with biological processes such as DNA repair or cellular death.

Therefore, the definition of total absorbed dose results weakened due to the time evolution of the cell culture, leading to the necessity of improving the existent approaches.
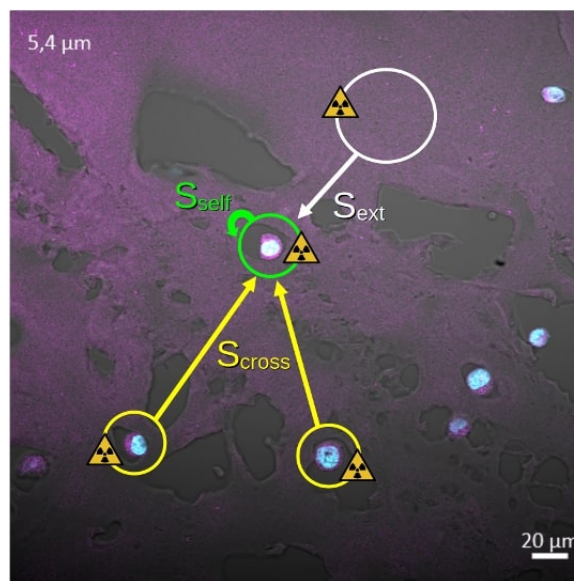


Figure 2.11: Cellular S-values depicted in a 3D cell culture administered with an unlabeled pharmaceutical (confocal microscopy).

It could be helpful to study the DNA damage by using the MIRD schema not only to compute the dose rate using dose S-values, as usual, but even for the damage rate itself. By associating the computed damage S-values to proper biophysical models, it will be possible to predict experimental results, as *foci* assays and cell survival. The *foci* technique is based on the phosphorylation of the protein H2AX, which is a component of DNA histones. After the occurrence of DNA breaks, this protein is phosphorylated to the $\gamma$-H2AX form, which can be detected by confocal microscopy. In combination with H2AX, another protein frequently utilized in *foci* assays is 53BP1. Unlike H2AX, 53BP1 is more specifically involved in the repair of double-strand DNA breaks (DSBs) and exhibits greater specificity for this type of DNA damage. By employing a combination of H2AX and 53BP1 proteins, it is possible to gather comprehensive information about the presence and localization of DNA damage within cells. As a matter of fact, the phosphorylation of H2AX provides a broader indication of DNA damage, encompassing various types of lesions, while the presence of 53BP1 *foci* allows for a more specific assessment of DSBs. This technique can be helpful as an experimental test for the validity of Geant4-DNA simulations because it provides a direct measurement of the extent and distribution of DNA damage induced by ionizing radiation. In order to compute the aforementioned S-values, the software Geant4-DNA has been employed.

# Chapter 3

# GEANT4-DNA

## 3.1 About GEANT4

GEANT4 is a highly sophisticated Monte Carlo simulation toolkit designed to meet the complex requirements of modern particle and nuclear physics experiments, as well as other disciplines where particle interactions are fundamental.

Monte Carlo simulation methods are a statistical approach to modeling complex systems that involve random processes. Applying to the case of GEANT4, this involves generating random numbers to simulate the interactions of particles with matter. This includes the probability of a particle being scattered or absorbed by the material it passes through, as well as its probability of emitting secondary particles. Even if Monte Carlo methods can require significant computational resources to model complex scenarios and setups, they offer exceptional accuracy and are considered an alternative to deterministic approaches. The mentioned methods, such as solving differential equations, are based on precise mathematical models and can provide exact solutions if the model accurately represents the system being studied. However, in many cases, the true behavior of the system is too complex to be represented by a deterministic model: Monte Carlo methods, on the other hand, can handle complex, stochastic systems by generating random numbers that represent the probability distributions of various physical processes.

Concerning the GEANT4 toolkit, it provides a comprehensive set of software components that cover all aspects of the simulation process, from the construction of the system's geometry to the tracking of particles passing through materials and external electromagnetic fields, to the physics processes governing particle interactions, along with the response of sensitive detector components. One of the most remarkable features of GEANT4 is its built-in steering routines and command interpreters, which provide a simple and intuitive way for users to define their simulation problems, configure the simulation parameters, and execute simulation runs. These tools are designed to work at various levels of the simulation process, from the initial problem setup up to the final analysis of the simulation results, allowing users to have complete control over the entire simulation process.



Figure 3.1: GEANT4 logo.

GEANT4's extensive set of physics models lies at the basis of the toolkit, making it possible to handle particle interactions across a wide energy range. These models have been sourced from numerous locations worldwide and are continually expanded and developed to keep up with the evolving requests

of particle physics research. The approach of the toolkit separates the physics processes from the models that describe them, allowing multiple independent models to exist for the same process, so that users can freely choose the models that best suit their needs, whether in terms of energy range, precision, or CPU time. The open system of physics in GEANT4 also enables users to create and incorporate their own customized models without difficulties. Thanks to the toolkit's flexibility and the availability of specialized physics models, such as those for low energy, it has gained widespread use in diverse experimental communities, from high-energy physics and accelerator physics to astroparticle physics, astrophysics, and medical physics.

## 3.2 Geant4-DNA

### 3.2.1 Overview

The GEANT4-DNA project is an extension of the general-purpose GEANT4 Monte Carlo simulation toolkit that focuses on simulating the interactions of ionizing radiation with biological systems at the molecular level. It provides a set of specific models useful to simulate the interactions of particles with biological molecules such as DNA, RNA, and proteins, as well as the subsequent chemical and biological processes that occur as a result.

Initiated in 2001 by Dr. P. Nieminen at the European Space Agency, the project aimed to develop a computing platform that could estimate the biological effects of ionizing radiation using the GEANT4 toolkit. A preliminary set of physical processes tailored to microdosimetry in liquid water and capable of operating down to the electronvolt scale was integrated into the GEANT4 toolkit in 2007. Since then, the GEANT4-DNA project has continued to refine and enhance these processes. The GEANT4-DNA collaboration brings together GEANT4 developers, who are members of the larger collaboration, as well as external consultants with expertise in theoretical elementary particle physics, radiolysis, and microdosimetry. The current collaborators of the GEANT4-DNA project are listed as authors of related publications, and the project is a full activity of the GEANT4 Low Energy Electromagnetic Physics Working Group. All ongoing developments are included in the public releases of the GEANT4 toolkit, ensuring that the latest enhancements are available to users worldwide. A dedicated website provides detailed descriptions of the project's developments, making it a valuable resource for researchers interested in simulating the interactions of ionizing radiation with biological systems at the molecular level.

Rather than developing a new Monte Carlo software that focuses only on microdosimetry and on the simulation of biological damage caused by radiation, the GEANT4-DNA project was born to be an expansion of the capabilities of the GEANT4 toolkit. This approach provides greater flexibility and efficiency in simulating the interactions of ionizing radiation with biological systems at the molecular level, so that researchers can have a single, comprehensive toolkit to simulate a wide range of biological systems and scenarios. Ultimately, this is frequently applied in the development of new radiation therapies and the understanding of the mechanisms of radiation damage to biological systems.

### 3.2.2 Models, physics processes and physics lists

GEANT4-DNA employs C++ "process classes" to calculate the total cross-sections of specific physical interactions, such as elastic scattering and ionization. These classes provide a detailed description of the interaction products, including kinematics, production of secondary particles and energy deposits. The physical interactions simulated in GEANT4-DNA are purely discrete, meaning that they are simulated step-by-step with precise tracking, without using any condensation technique. The user can compute physical quantities based on a variety of models, either theoretical or semi-empirical, using dedicated "model classes". These classes can be complementary in energy ranges or completely alternative, and any single process class can evoke one or several of them.

GEANT4-DNA covers the dominant interactions of light particles and ions, including electrons, protons, hydrogen, helium particles, and their charged states, reaching the electronvolt scale in liquid water, which is the primary component of biological matter. Some models are purely analytical, while others

use interpolated cross-section data tables for faster computation.

To simulate the interactions of particles with matter in a GEANT4 user application, the user needs to specify the particles and the corresponding physical processes affecting these particles in a dedicated "physics list" class. For instance, in the case of simulations in liquid water, the recommended physics lists follow:

- **G4EmDNAPhysics_option2**: it is an accelerated default constructor that simulates electron interactions up to 1 MeV, as well as all other particle interactions. It is a faster option compared to other physics lists, and is suitable for simulations where simulation speed is a priority;

- **G4EmDNAPhysics_option4**: it includes electron elastic and inelastic models developed by D. Emfietzoglou, I. Kyriakou, S. Incerti [28], and is valid for electron energies up to 10 keV. This option is suitable for simulations that focus on low-energy electrons;

- **G4EmDNAPhysics_option6**: it includes CPA100 electron elastic and inelastic models developed by M. C. Bordage, M. Terrissol, S. Incerti [28], and is valid for electron energies up to 255 keV. This option is suitable for simulations that focus on intermediate-energy electrons.

### 3.2.3 Models for direct DNA damaging

GEANT4-DNA includes physical processes and models that are integrated into the GEANT4 toolkit, allowing for the combination of GEANT4's geometry modeling capabilities with GEANT4-DNA's physical processes. This enables the creation of high-resolution geometries for biological targets with sub-micrometer scale resolution. These geometries represent a significant improvement over previous GEANT4 geometrical models used for dosimetry studies at the biological cell. There are two approaches to implementing high-resolution geometries:

- **Voxellized approach**: uses reconstructed 3D images acquired using high-resolution imaging techniques (such as confocal microscopy) to develop high-resolution cellular phantom geometrical models at the sub-micrometer scale, representing realistic individual human keratinocyte cells, including the cell nucleus, inner nucleoli, and cytoplasm. These phantoms enable more precise dosimetry calculations in cellular irradiation experiments involving single-ion microbeams. The physical calculations are performed using GEANT4's low-energy electromagnetic processes.

- **Atomistic approach**: to achieve higher resolution, biological targets at the nanometer scale, such as the DNA molecule, are modeled using combinations of basic mathematical volumes. Taking inspiration from he work of M. A. Bernal and J. A. Liendo in their investigation of the capabilities of the PENELOPE Monte Carlo code in nanodosimetry, the model has 4 geometry levels: deoxynucleotide pairs, DNA double helix, nucleosomes (which comprise two DNA loops wrapped around a chromosomal protein called histone), and chromatin fiber (which represents the DNA assembled into chromosomes). Implementing this geometrical model into a GEANT4 application can be done in a "top-to-bottom" order, starting from the chromatin fiber and moving down to the DNA bases. This approach takes advantage of the geometrical symmetries of the model, eliminating the need to implement each individual deoxynucleotide pair into the program. Particles can be sent on the fiber, and the location of each elementary energy deposit in the particle shower can be accurately determined and recorded in the geometry. Targets within the model, identified by their respective slice, nucleosome, and DNA helix loop, can be assessed to estimate the number of DNA SSBs and DSBs induced by the incident ionizing particle. These strand breaks are considered as one of the basic observable forms of biological damage.

### 3.2.4 Models for indirect DNA damaging

Ionizing radiation can cause direct damage to the DNA molecule by transferring sufficient energy to generate strand breaks, which typically occurs within the first $10^{-15}$ seconds after the primary ionizing particle penetrates into a biological cell. However, direct interaction with ionizing radiation is not the main mechanism for DNA damage caused by low-LET radiation. Instead, most damage is induced by the indirect effects of ionizing radiation, which occur between $10^{-15}$ and $10^{-12}$ seconds. During

this stage, water molecules that were previously ionized and excited may de-excite and dissociate, generating molecular radical species. These reactive species diffuse through the surrounding medium, interacting with water molecules and DNA, and are responsible for most of the damage to the DNA molecule. [28]

## 3.3 The molecularDNA example

As described in [29], the "molecularDNA" example of Geant4-DNA has been included in the extended examples category of Geant4 public release 11.1 BETA (released in June 2022). "molecularDNA" is a Geant4-DNA example built to allow easy simulation of radiation-induced DNA damage with flexible geometries and well defined damage parameters. This example includes three different DNA-scale designs of biological targets, fully described in the following paragraphs.

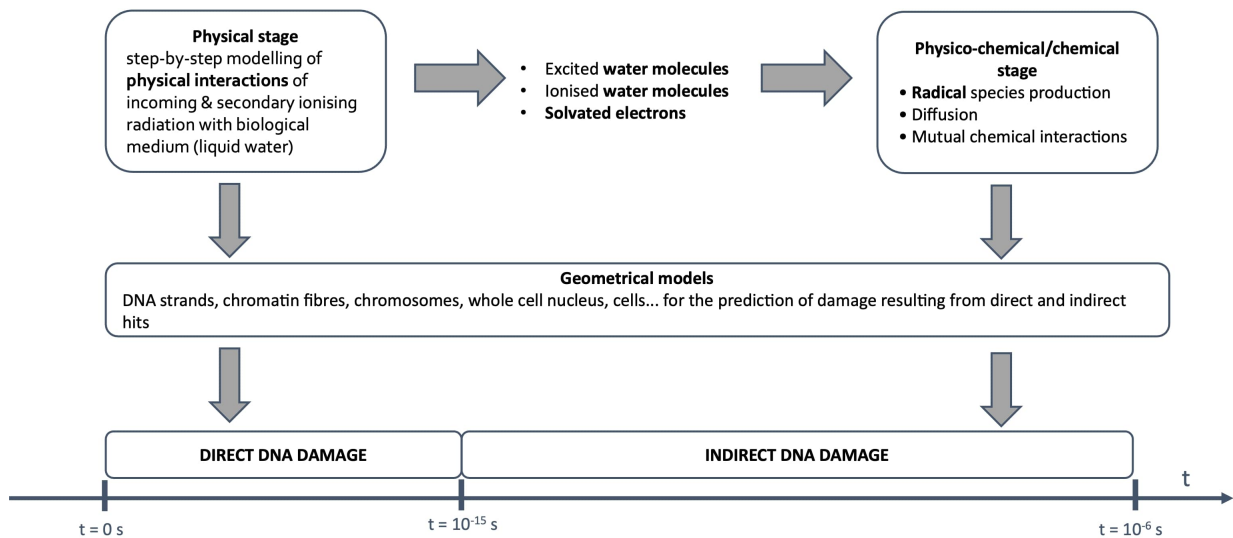The scheme represented in Fig. 3.2 explains the simulation process:



Figure 3.2: Scheme of the simulation's principle of work.

The simulation process involves two stages: the physical stage and the physico-chemical stage.

- In the **physical stage**, Geant4-DNA simulates the transport of the ionizing particles through the biological medium, taking into account the energy loss and scattering of the particles due to interactions with the medium. The transport is modeled by the Monte Carlo method, which uses random numbers to simulate the stochastic nature of the particle interactions.

- In the **physico-chemical stage**, Geant4-DNA simulates the subsequent chemical and biological processes that occur as a result of the initial ionizing event. This includes the diffusion and reaction of the reactive species with other biological molecules, such as proteins and lipids, and the repair or misrepair of DNA damage.

The time scale of the simulation can range from femtoseconds, when initial ionization events occur, to hours, since the repair of DNA damage can take hours to complete.

**Cylinders** The cylinders geometry (see Fig. 3.3) implemented in the molecularDNA example was inspired by Charlton et al. [30] and first implemented by Nikjoo et al. [31]. This simple geometry, chosen to explore the relationship between physical damage and its influencing parameters, consists of cylinders filled with DNA at random positions and directions. It allows users to calculate the number of radicals produced due to the interaction of radiation with water, known as the radiolysis process. More precisely, the geometry consist of a 3 $\mu$m radius water sphere filled with 200,000 individual 216 base-pair-long straight DNA segments, each inside a cylindrical volume of 15 nm radius and 100 nm height [28].
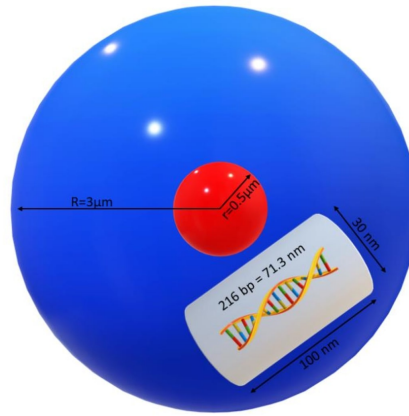
Figure 3.3: Schematic representation of the "cylinders" geometry. A large water sphere (blue sphere in the figure) contains 200,000 cylinders including 216 bp of DNA as shown (in magnification) in the right-hand side corner. The red sphere represents the source geometry, in this case 4.5 keV monoenergetic electrons. Image from [29].

**E. coli**    In the molecularDNA example, the geometry of the Escherichia coli bacterium genome (see Fig. 3.4) is modeled using a unique approach. Specifically, the geometry is represented through the use of four side-by-side Hilbert curve fractals, as described in the scientific literature [28]. Hilbert curve fractals are a mathematical construct that enables the creation of complex patterns and shapes through an iterative process of replacing each line segment with a smaller, scaled version of the original curve. The use of this approach allows for a more realistic representation of the intricate and irregular shape of DNA, which is critical for analyzing the complex processes of DNA damage and repair.
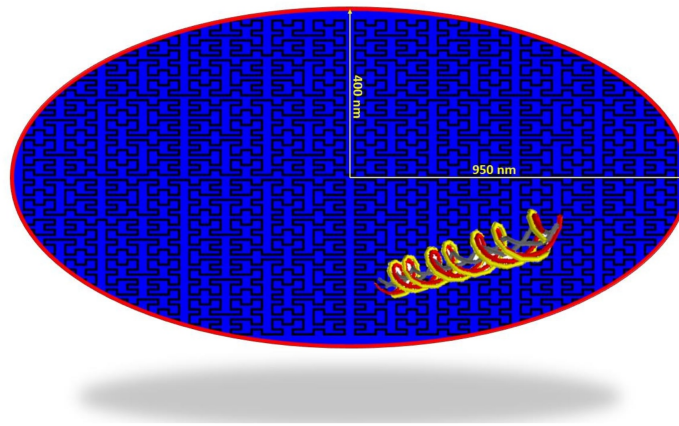


Figure 3.4: Simplistic 2D representation of "E. coli" geometry. The black lines inside the ellipsoid water cell represent the fractal path of DNA (Hilbert curve). A segment of E. coli DNA is shown in the right-hand side corner (not in scale with the rest of the geometry in the figure). The red line around represents the source of radiation. Image from [29].

To model the DNA geometry of an E. coli bacterium, four side-by-side fractals are used, with each fractal representing a section of the genome. They are arranged in a way that represents the overall shape of the bacterium and are then used to create placement volumes representing the physical location of the DNA segments within the genome, which are modeled as cubic boxes with a side length of 50 nm. To simulate the size of the bacterium, only the volumes placed inside an ellipsoid with semi-length of axes dimensions of 950 nm x 400 nm x 400 nm are considered, ensuring that the final geometry simulates the overall size and shape of an E. coli bacterium. The final geometry contains

4.63 Mbp[1] of DNA, with 3,600 straight and 5,625 turned segments of DNA, nearly identical in size to the E. coli genome. By using Hilbert curve fractals to create the DNA geometry, the simulation allows for a highly detailed and realistic 3D model of the E. coli genome, which can be used to study the effects of radiation on the DNA segments within the genome, providing insights into the mechanisms of radiation-induced DNA damage.

**Human cell**    The last geometry (see Fig. 3.5) is a representation of a human fibroblast in which the DNA is represented by a **continuous Hilbert curve fractal-based DNA chain** composed of chromatin sections, including **histones**.
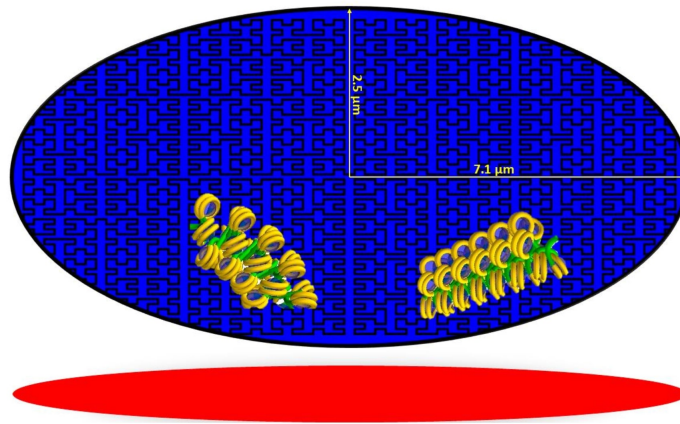


Figure 3.5: Simplistic 2D representation of "Human cell" geometry. The black lines inside the ellipsoid water cell represent the fractal path of DNA (Hilbert curve). A segment of E. coli DNA is shown in the right-hand side corner (not in scale with the rest of the geometry in the figure). The red disk represents the source of radiation. Image from [29].

The chromatin sections in the DNA chain were modeled as straight and turned to reflect the natural variability in the shape and structure of chromatin in real cells. By including histones in the simulation, the model is able to provide a more realistic representation of the DNA structure within the cell, which is essential for accurately modeling the effects of radiation on DNA. The continuous DNA chain structure is approximately 6.4 Gbp long and is placed inside an ellipsoid of 7.1 $\mu$m x 2.5 $\mu$m x 7.1 $\mu$m semi-axes that imitates the human cell nucleus as shown in Fig. 3.5. This setup results in an effective nucleus density of approximately 0.015 bp/nm$^3$.[29]
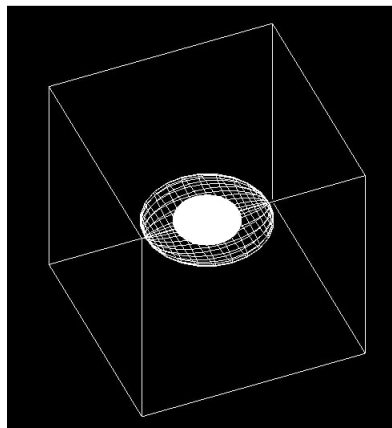


Figure 3.6: Screenshot of the human cell geometry simulated on OGLQt.

---

[1]Standing for "Mega base pairs", this unit of measurement is frequently used in genomics and molecular biology to quantify the length or size of DNA molecules. In particular, a base pair consists of two nucleotide bases bonded together in the DNA double helix.

### 3.3.1   DNA geometry

When simulating the behavior of DNA, it is important to take into account its complex double helix structure. To simplify this process, Lampe et al. [32] proposed a geometric model of DNA based on a fractal structure (see Fig. 3.7). Fractals are mathematical patterns that repeat themselves at different scales, and they can be used to create complex structures with self-similar properties. In this case, a Python script was used to generate the fractal geometry, allowing for flexibility in constructing the overall structure. By adjusting the initial curve from which the fractal was seeded, the researchers were able to create a simplified model of DNA that captured its essential features and behavior. The DNA geometry is constructed in two steps: the first describes the geometrical arrangement of the nucleotide bases and the sugar-phosphate backbone in a curved or straight chromatin segment, while the second represents the overarching macrostructure of the DNA.
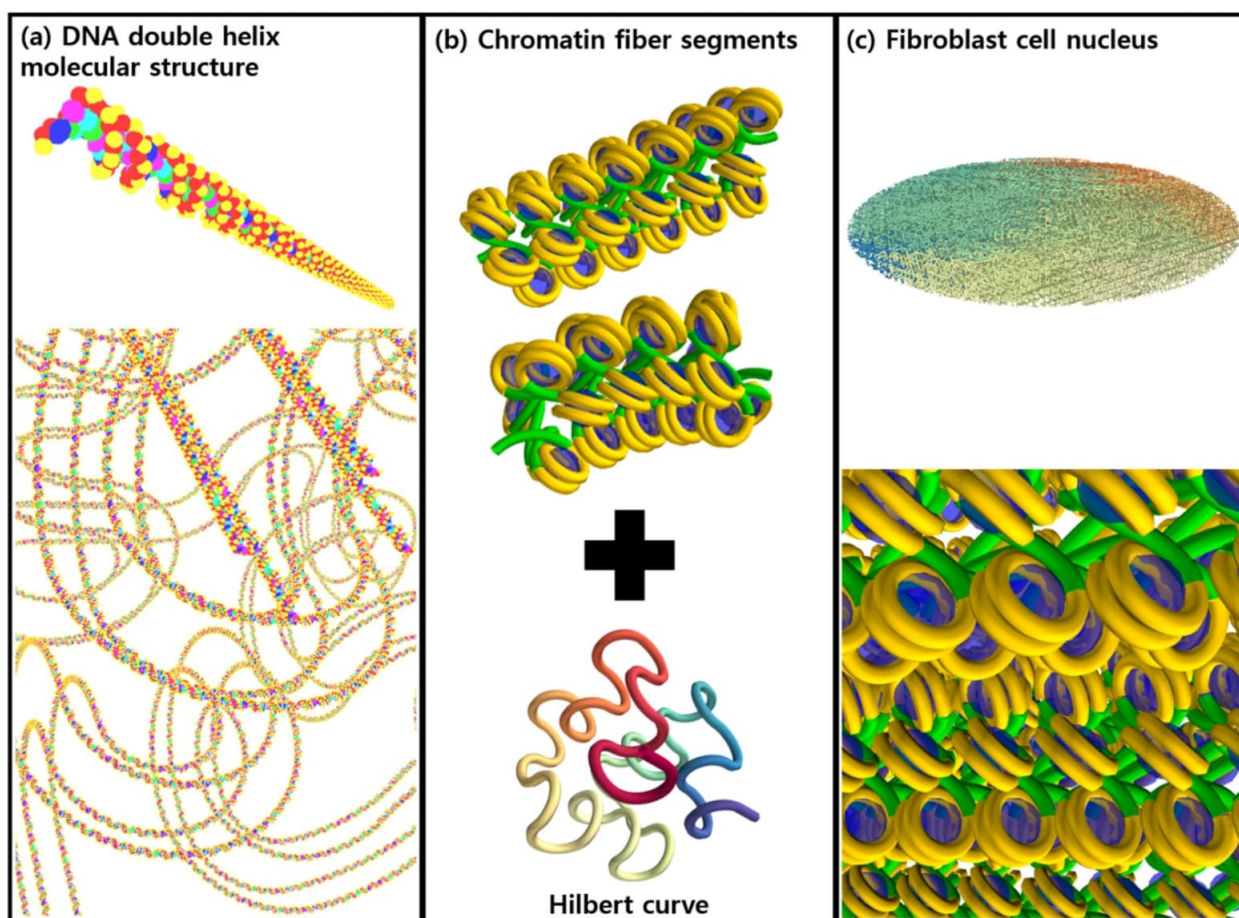


Figure 3.7: (a) A schematic illustration depicting the molecular structure of the DNA double helix is shown. The spheres represent different components of the DNA molecule, including adenine (C5H5N5, blue), thymine (C5H6N2O2, magenta), guanine (C5H5N5O, green), cytosine (C4H5N3O, cyan), sugar (C5H10O4, deoxyribose, red), and phosphate (H3PO4, yellow). (b) Simplified chromatin fiber segments (straight and turned) and a unit of Hilbert curve are displayed. (c) Model of the fibroblast cell nucleus. Image from [33].

To construct realistic inter-linked chromatin segments, three geometries for segment models were produced: straight, turned and turned-twisted. The straight segment model represents a linear arrangement of the chromatin fiber, while the turned segment model represents a curved or bent configuration. The turned-twisted segment model, on the other hand, represents a more complex arrangement that combines both bending and twisting of the chromatin fiber. The fractal structure of the chromosome was generated from the Hilbert curve, which is typically used for continuous fractal space-filling. The iteration of the Hilbert curve resulted in a more complex and continuous chromatin fiber. To shape the cell nucleus, a spherical or ellipsoidal mask was used, depending on the cell geometry.[32][33]

### 3.3.2 DNA-damage classification

DNA damages were classified according their complexity, in particular:

- **SSB**: single break on a DNA strand;

- **DSB**: two breaks on opposite strands that were simultaneously induced within the distance $d_{DSB}$, set at $d_{DSB} = 10$ bp (base pairs). This means that if the 2 breaks happened at a distance larger than $d_{DSB}$, they are considered as independent SSBs;

- **Complex SSBs**: by considering a fragment gap $d_s = 100$ bp, SSB+ represents damages on the same strand, while 2SSB represents damages on opposite strands;

- **Complex DSBs**: DSB+ classification requires one DSB damage and one more break within $d_{DSB}$, while DSB++ requires 2 DSBs within $d_s = 100$ bp. These damages are more important compared to the previous ones since they cause irreparable DNA damage in further calculations.

Moreover, it has been classified single-strand breaks (SSBs) and double-strand breaks (DSBs) as **direct damage** ($SSB_d$ and $DSB_d$) or **indirect damage** ($SSB_i$ and $DSB_i$). Direct damage was defined as damage that occurred directly to the DNA molecule, while indirect damage was caused by reactive oxygen species that were produced by the ionizing radiation. More complex classification are provided, including **mixed damage** ($SSB_m$, $DSB_m$), which is scored when both direct and indirect breaks are involved, and **hybrid damage** ($DSB_{hyb}$), which refers to a DSB that consists of at least one segment containing both indirect and direct damages. In order to determine whether energy deposition affects DNA, giving a direct kind of damage, it is necessary to define an effective target volume and radius: to account for the energy depositions in the hydration shells of sugar and phospate, GEANT4-DNA utilized an effective radius, $R_{direct}$, which was set to be larger than the van der Waals radius of these molecules (2.28 Å and 2.63 Å, respectively). In Fig. 3.8, DSB damage were represented by considering both their complexity and the source of the damage.[32][34]
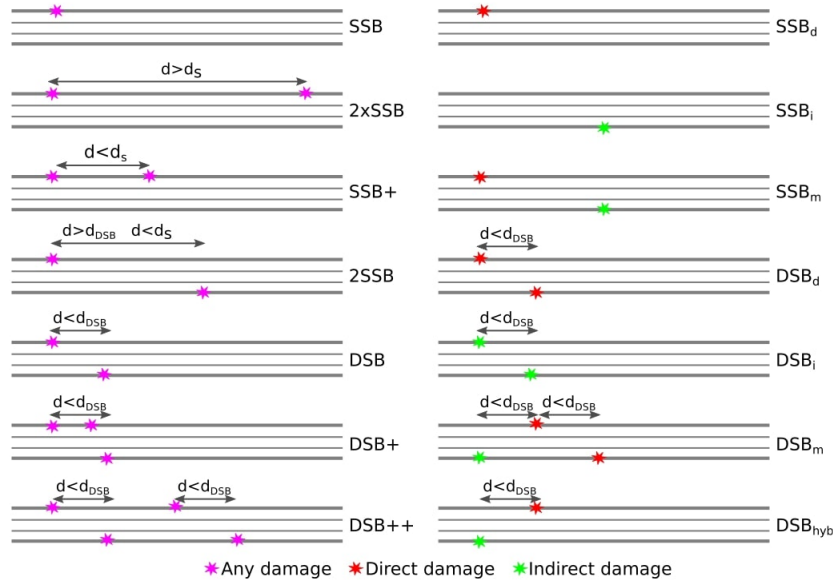


Figure 3.8: The scheme of classification for complexity (left) and for source (right) of SSB and DSB. [32]

# Part II

# Analysis of the results

# Chapter 4

# Damage S-Values

Considering the expected computational weight of this kind of simulations for a complex system, a preliminary evaluation of the minimum required statistics of generated events was performed. To do so, simulations were run with an increasing number of events in order to determine the point at which the results become enough stable and reliable. By comparing the results coming from a shorter simulation to those obtained from a much longer one, which is considered to have reached the "true values", it is possible to determine how many events are needed to simulate data with a sufficient level of accuracy. This process helps to limit the impact of statistical noise or fluctuations on the final results. For this reason, the first step of the performed analysis is based on determining the minimum number of events needed to generate accurate results, thereby reducing the computational cost of simulations while maintaining their accuracy.

Two distinct source distributions are considered (see Fig. 4.1):

- The **superficial** distribution, in which the source is distributed on the detecting cell membrane;

- The **volumetric** distribution, in which the source is internalized inside the volume of the detecting cell.
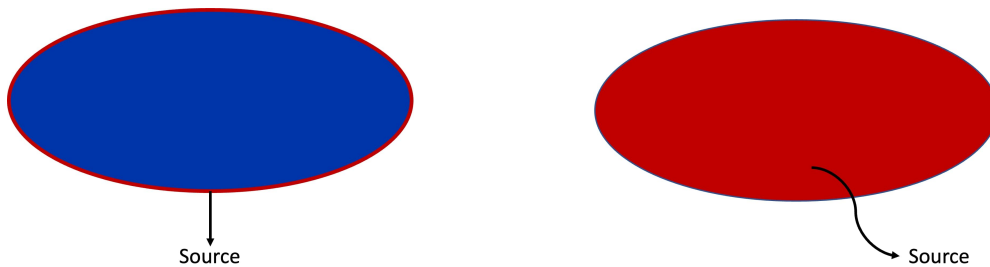


Figure 4.1: Schematic representation of the geometries used for the two source distribution.

These distributions allow for an exploration of the effects of different source distributions of interest on the resulting rates of DNA damage.

## 4.1 Analysis conducted on E. Coli geometry

To begin with, the chosen approach focuses on applying the simulation procedure specifically to the E. Coli geometry. This decision is driven by the fact that simulations conducted on the bacterial geometry are characterized by a faster computation time compared to the ones generating the more complex human cell geometry. In these simulations, monoenergetic electrons are set as source, with their energy levels gradually increasing from 100 keV up to 1 MeV. The graphs shown in Fig. 4.2 represent the total rates of single strand breaks and double strand breaks as a function of the energy

levels of the electrons used in each simulation. Moreover, it has been investigated the influence of the number of events launched during the simulations on the observed rates of SSBs and DSBs and on their distribution among the energies.
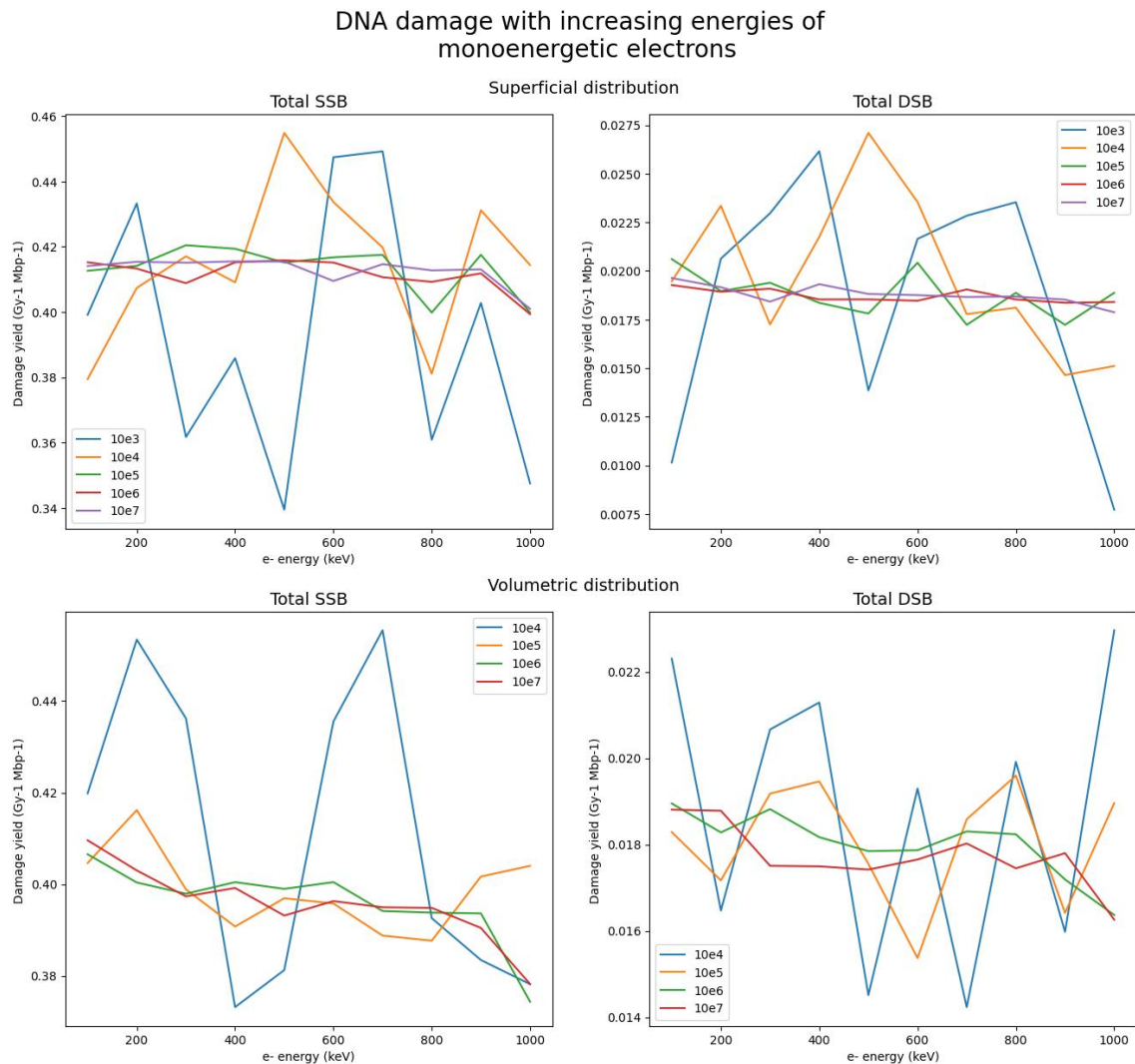


Figure 4.2: SSB and DSB rates depending on the energy, represented for each simulation changing the number of events.

Fig. 4.2 shows that as the number of events increases, the SSB and DSB rates become more stable and consistent across different electron energies. This is easy to notice by looking at the trend lines, which are clearly becoming flatter with the increase of the number of events. This result suggests that the simulation outputs are progressively converging towards a stable value.

The stability of the results obtained by increasing the number of events is likely due to the reduction of statistical noise or fluctuations that can arise from the stochastic nature of radiation-matter interactions.

Subsequently, in order to assess the reliability of the results, the SSB and DSB rates obtained from simulations with less than $10^7$ events are compared to the "true values" obtained from the longest simulation. The percentual residuals are then calculated as

$$\text{Residual} = 1 - \frac{\text{Simulated value}}{\text{True value}}$$
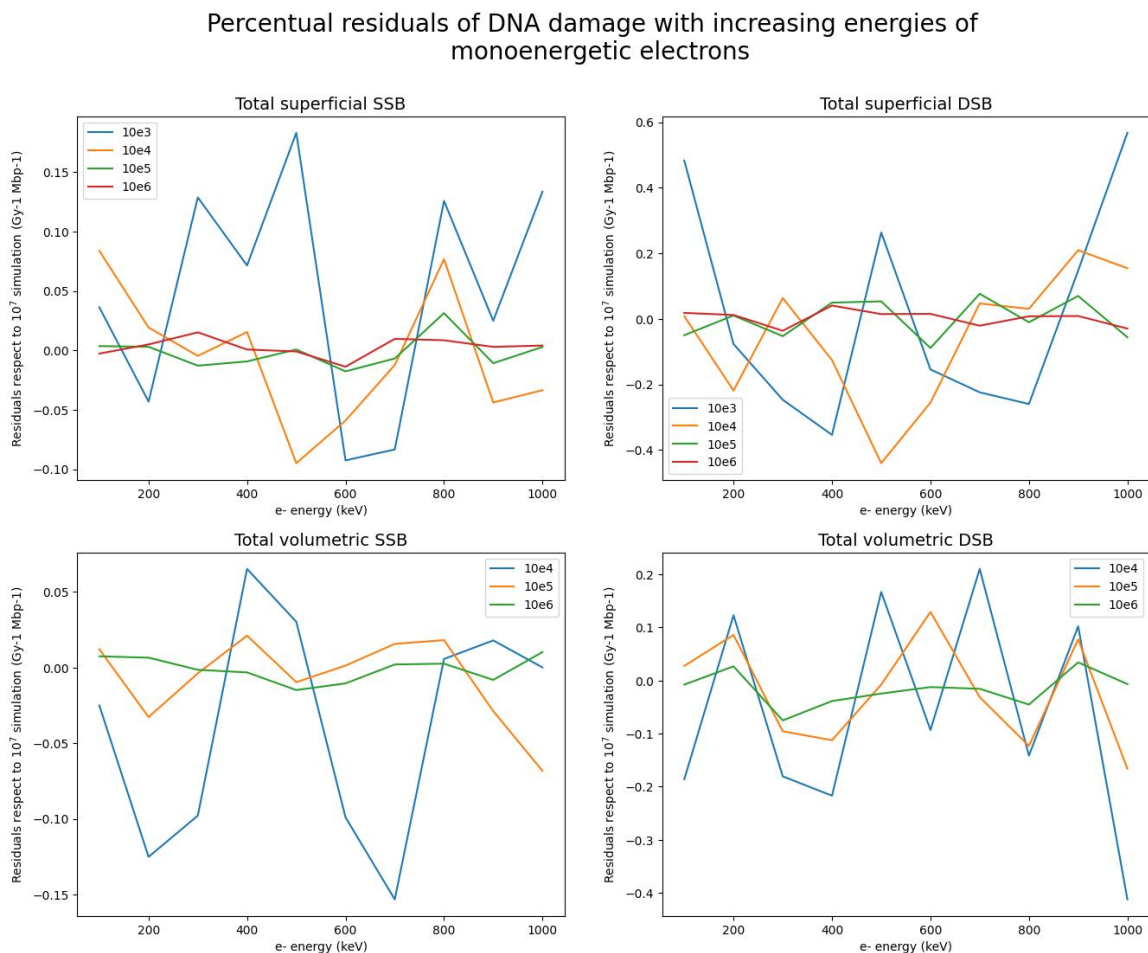
and are shown in Fig. 4.3.



Figure 4.3: Percentual residuals of SSB and DSB results depending on the energy, represented for each simulation changing the number of events.

Finally, it is important to confirm whether simulations with $10^6$ events give reliable results, which would lead to a great compromise between time needed for the simulation and precision of the results. In order to perform this final analysis, the standard deviation respect to the longest simulation of $10^7$ events is computed and plotted in Fig. 4.4. As one can clearly notice in Tab. 4.1 and Tab. 4.2 , shorter simulations do not guarantee reliable results due to the fact that the standard deviation is over 8%, while for simulations with $10^6$ events it results less than 1%.

The reason why the volumetric plot shows one point less compared to the superficial one is due to the fact that $10^3$ events are not enough even to get damages.

On the other hand, simulations consisting of $10^6$ events demonstrate a standard deviation of less than

Table 4.1: Standard deviation results for superficial source distribution.

| N of events | $10^3$ | $10^4$ | $10^5$ | $10^6$ |
|---|---|---|---|---|
| SSB | 0.092 | 0.054 | 0.013 | 0.008 |
| DSB | 0.313 | 0.192 | 0.057 | 0.023 |

Table 4.2: Standard deviation results for volumetric source distribution.

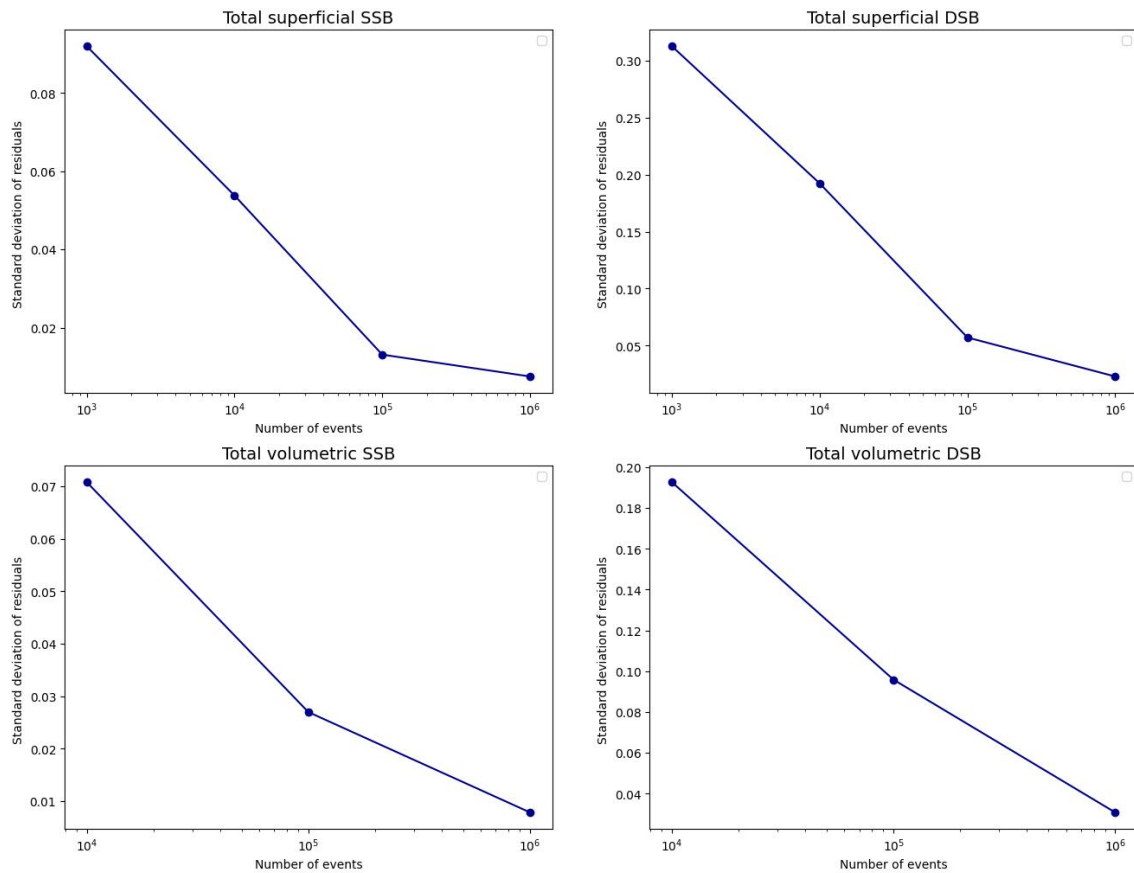| N of events | $10^4$ | $10^5$ | $10^6$ |
|---|---|---|---|
| SSB | 0.071 | 0.027 | 0.008 |
| DSB | 0.193 | 0.096 | 0.031 |



Figure 4.4: Standard deviation of residuals of SSB and DSB results depending on the energy, represented for each simulation changing the number of events

1% for SSBs and around 3% for DSBs. These findings confirm a higher level of precision and satis-factory reliability. It is important to note that DSBs occur less frequently than SSBs, and achieving greater precision necessitates a larger number of events, consequently leading to longer simulation times. Nevertheless, the obtained values exhibit a sufficient level of accuracy.

It should be noted that the volumetric plot exhibits one fewer data point compared to the surface plot. This discrepancy arises from the insufficient number of $10^3$ events, which proves inadequate for accurate damage assessment.

It is worth showing graphically the comparison between damages given by volumetric and superficial source distributions. As shown in Fig. 4.5, the DSB and SSB damage yields result higher when the source is distributed all over the cell surface compared to when it is internalized. The higher dose deposit inside the nucleus is probably connected only to geometrical reasons.
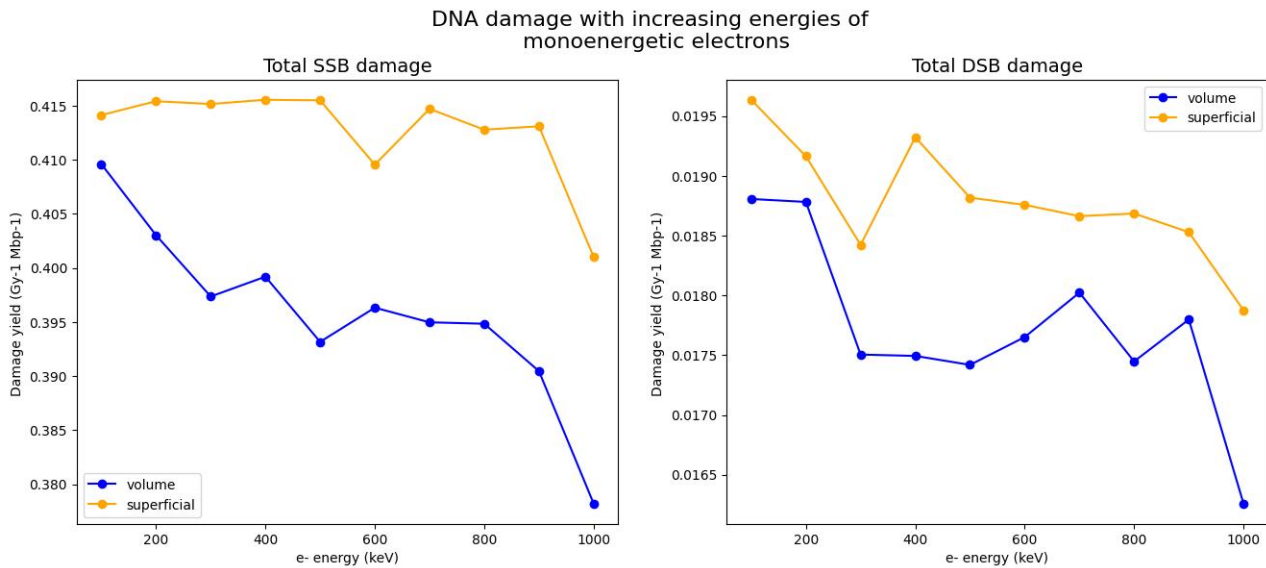


Figure 4.5: Comparison between damages of two source distributions considering $10^7$ events.

## 4.2 Analysis conducted on human cell geometry

**Cellular distributions** A similar stability analysis has been conducted using the human cell geometry and a source of $^{111}$Ag for the two distributions previously described. In this case, the simulations were launched several times, increasing the number of events but maintaining the same source. As mentioned, the simulations with the fibroblast geometry require higher computational times compared to the ones with the E. Coli geometry: this is why it has been decided to consider simulations with maximum number of events equal to $10^6$. The results are shown in Fig. 4.6 and Fig. 4.7:
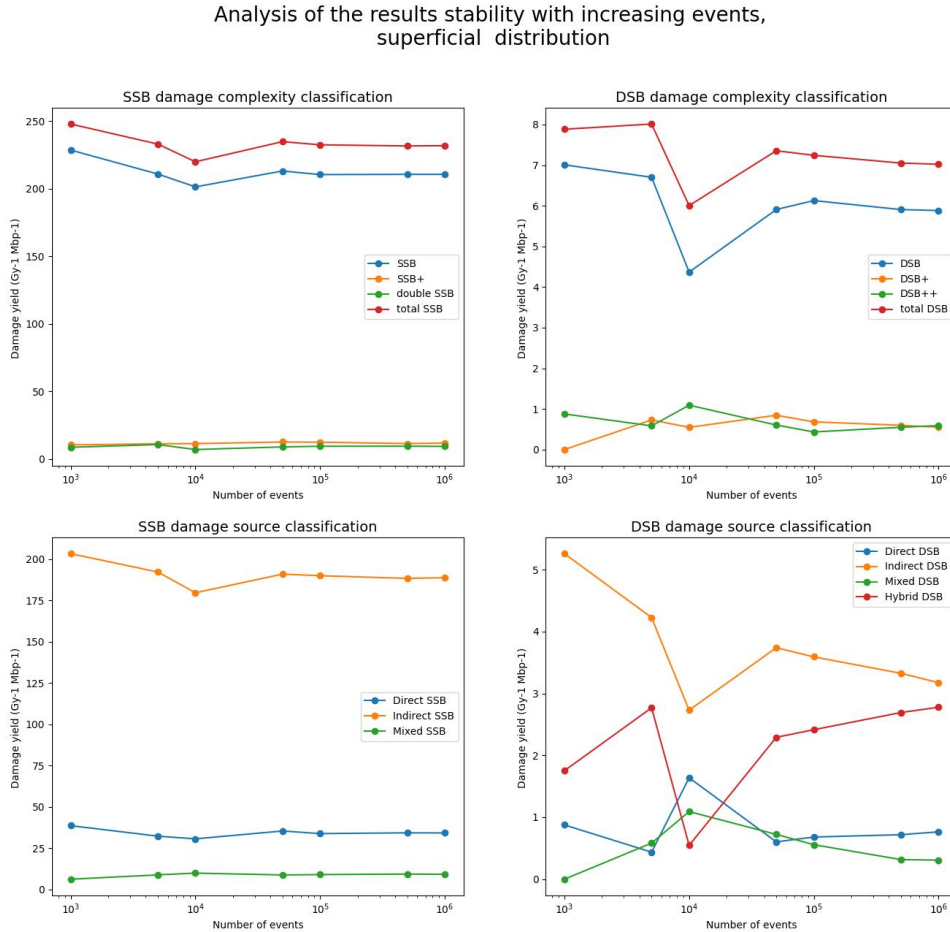


Figure 4.6: Plots of SSB and DSB damages for $^{111}$Ag superficial source with increasing number of events. On the top row the damage is classified by level of complexity. On the bottom row the classification is based on the damage source.

It is evident that points with higher event numbers exhibit a flatter trend compared to the ones with lower event numbers, thus confirming the progressive reaching of stability for the results. As a matter of fact, since the simulation remains consistent while only the number of events changes, normalizing to the dose (which shows a linear trend with the number of events, see Fig. 4.8) should give always the same results whenever the statistical sample is sufficient, graphically resulting in a flat line.
Due to the fact that the simulations took too much time to complete and it was possible to simulate up to $10^6$ events, small fluctuations are still visible, in particular for less frequent damage types.
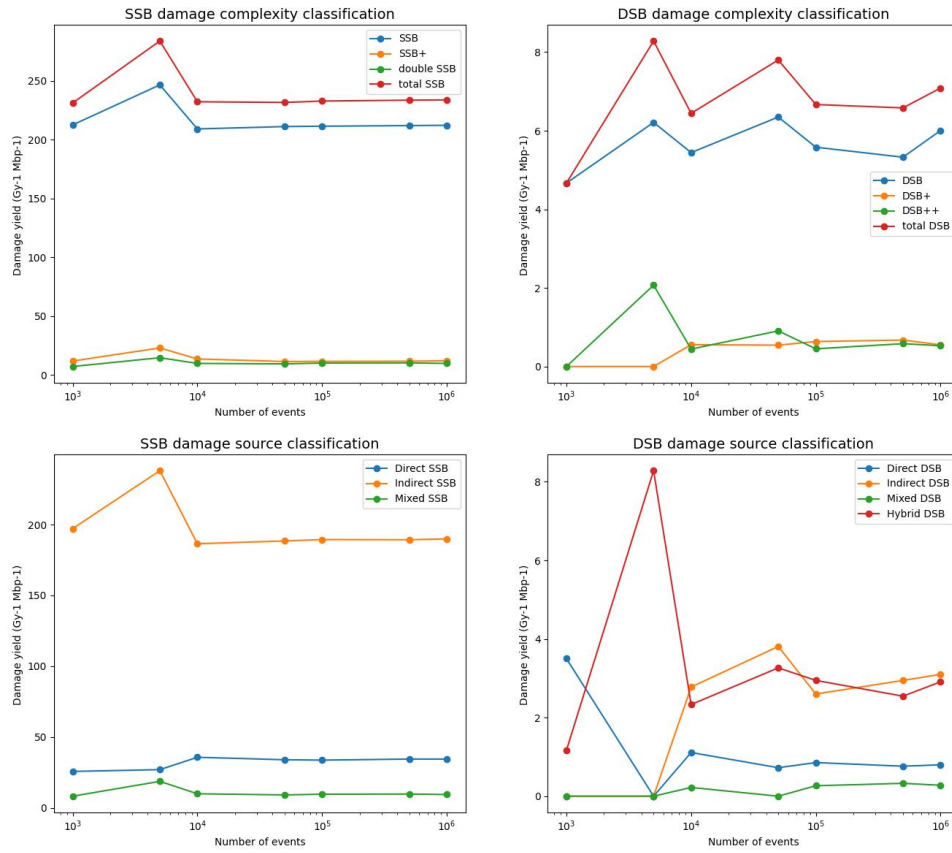
Figure 4.7: Plots of SSB and DSB damages for superficial distribution, $^{111}$Ag superficial source with increasing number of events. On the top row the damage is classified by level of complexity. On the bottom row the classification is based on the damage source.
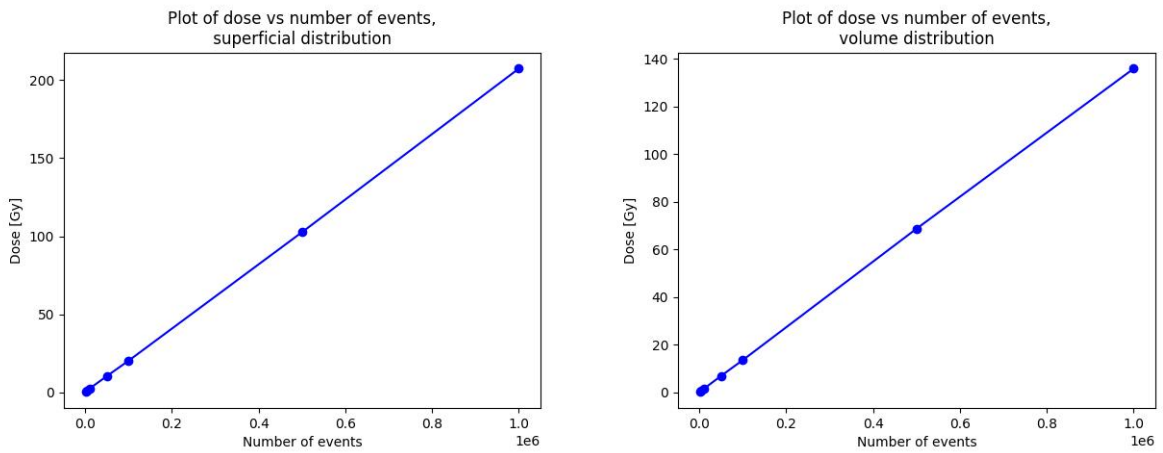


Figure 4.8: Dose plot for superficial and volumetric distribution.

### 4.2.1   Results with $^{111}$Ag

The main results regarding $^{111}$Ag are represented in Fig. 4.9 and Fig. 4.10, thus giving a clear representation of the extent of damage inflicted to cells in both source's geometrical configurations in the most stable case ($10^6$ events):
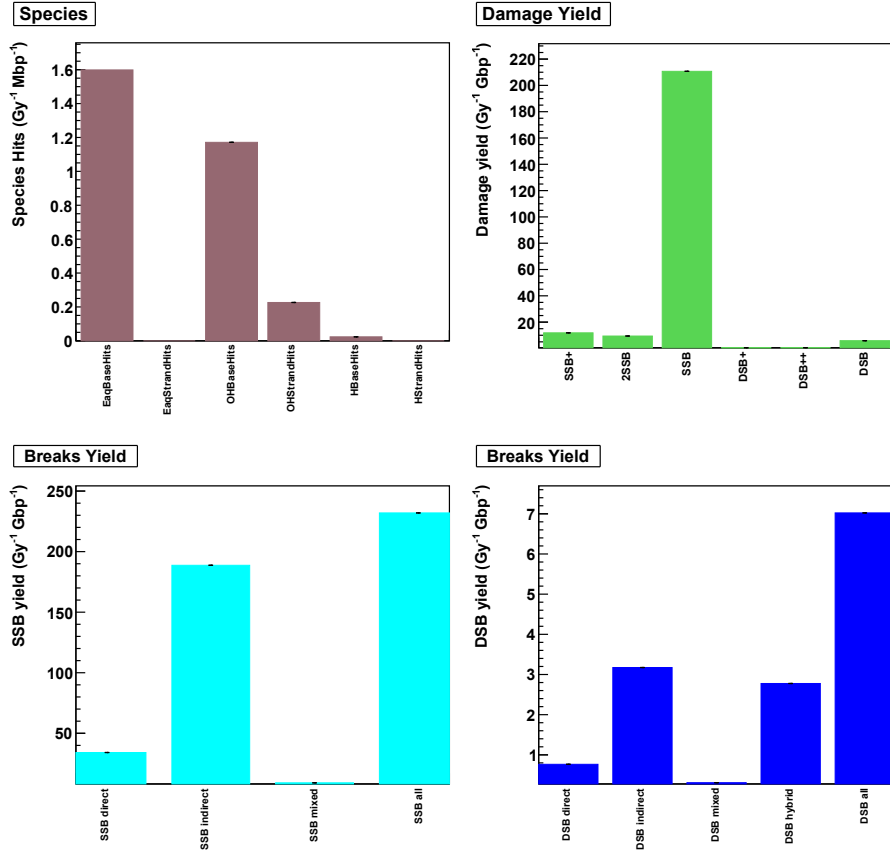


Figure 4.9: Histograms representing the main damage yields for $^{111}$Ag with superficial distribution.

To summarize, Tab. 4.3 shows the comparison between the main damage quantities resulting from the simulations with $10^6$ events for both the two $^{111}$Ag distributions:

Table 4.3: Dose absorbed by human cell with $^{111}$Ag source and $10^6$ events.

| Source distribution | Superficial | Volumetric |
|---|---|---|
| Dose absorbed [Gy] | 207 | 136 |
| Total SSB [Gy$^{-1}$ Mbp$^{-1}$] | 232 | 234 |
| Total DSB [Gy$^{-1}$ Mbp$^{-1}$] | 7.02 | 7.09 |

The outputs confirm, as noted previously, the higher damage yields characterizing simulations with the source superficially distributed compared to those derived from simulations with the volumetric distribution of the source.

The obtained results hold fundamental importance. In fact, the computed S-values can be used for the development of models that will be applied to *in vitro* studies with $^{111}$Ag source.
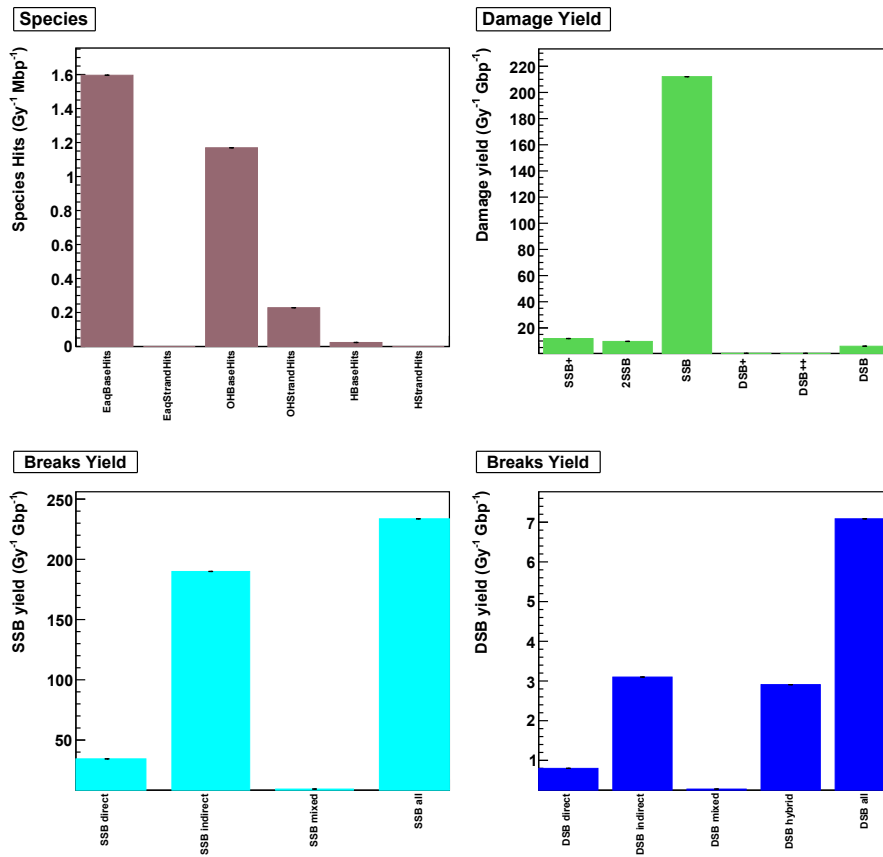
Figure 4.10: Histograms representing the main damage yields for $^{111}$Ag with volumetric distribution.

**Crossfire distribution**   In order to evaluate the influence of the surrounding environment on the detecting cell, another source geometry of interest is considered (see Fig. 4.11). Specifically, ellipsoidal volumes of water with the dimensions of the human cell geometry already simulated as detecting cell are used as source and progressively moved along the x-axis of 1 diameter steps from the detector.
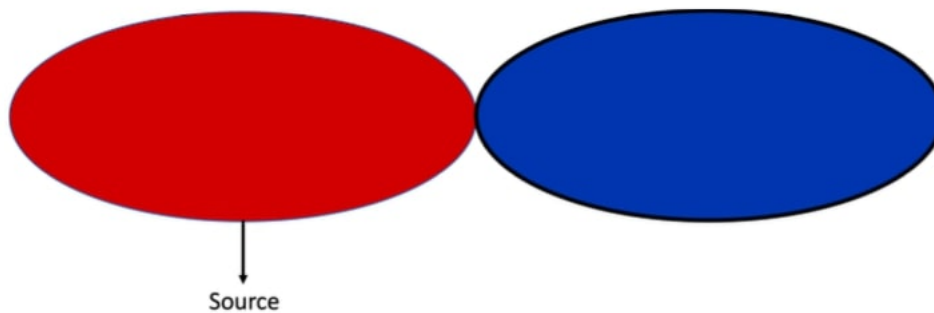


Figure 4.11: Schematic representation of the crossfire distribution. On the left, the red ellipsoid represents the source distribution, while the blue ellipsoid on the right represents the detecting cell.

The obtained result for the dose absorbed by the detecting cell behaves as shown in Fig. 4.12:
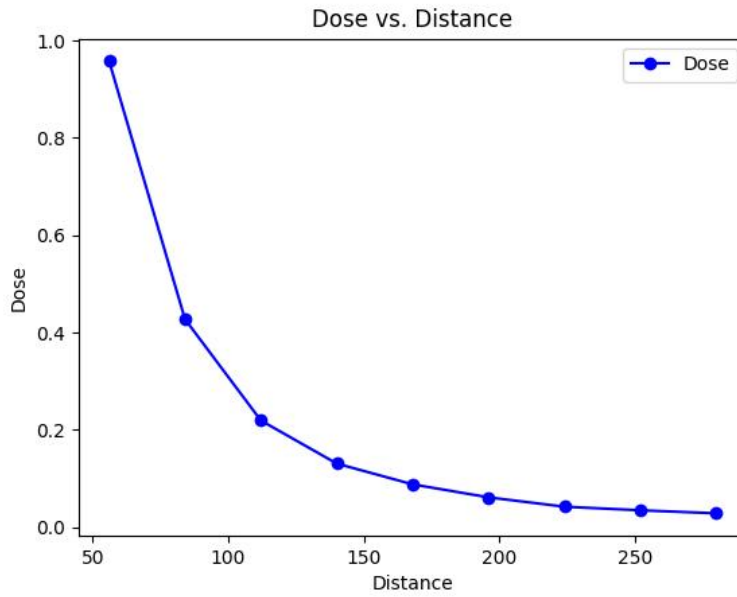


Figure 4.12: Dose plot of crossfire distribution.

As one can anticipate, due to the increasing distance between the source cell and the detecting one, the dose progressively decreases. This is because the radiation is distributed over a larger solid angle when the source is distanced, leading to less radiation reaching the target. The same decreasing trend is found when plotting the SSBs and DSBs in function of the distance between the source cell and the detecting cell, as shown in Fig. 4.13:



Figure 4.13: Damage plot of crossfire distribution.

Small fluctuations are probably due to the fact that the statistic was not sufficient: as a matter of fact, when the source is moved farther away, fewer events hit the cell's DNA. For this reason, it is expected that to have reliable results even the number of launched events has to be increased.

# Chapter 5

# $\gamma$-H2AX/53BP1 *foci* assay

## 5.1 DSB repair, detection, and quantification

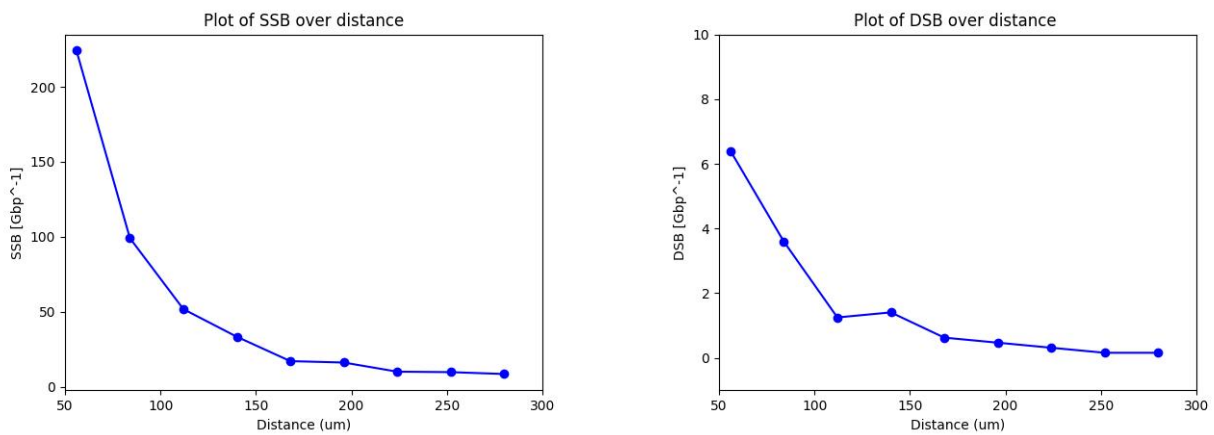As mentioned before, DSBs are the most significant DNA damages induced by radiation. Due to this fact, many studies have focused on the DSB repair mechanisms (see Sec. 1.1). To fully understand the subsequent analysis, it is essential to clarify the roles of two frequently employed proteins in DSB analysis: the phosphorylated histone $\gamma$-H2AX and the protein 53BP1.

### 5.1.1 H2AX

H2AX is a variant of the H2A protein family, a component of the histone octamer forming the structural units of chromatin, called nucleosomes (Fig. 5.1).
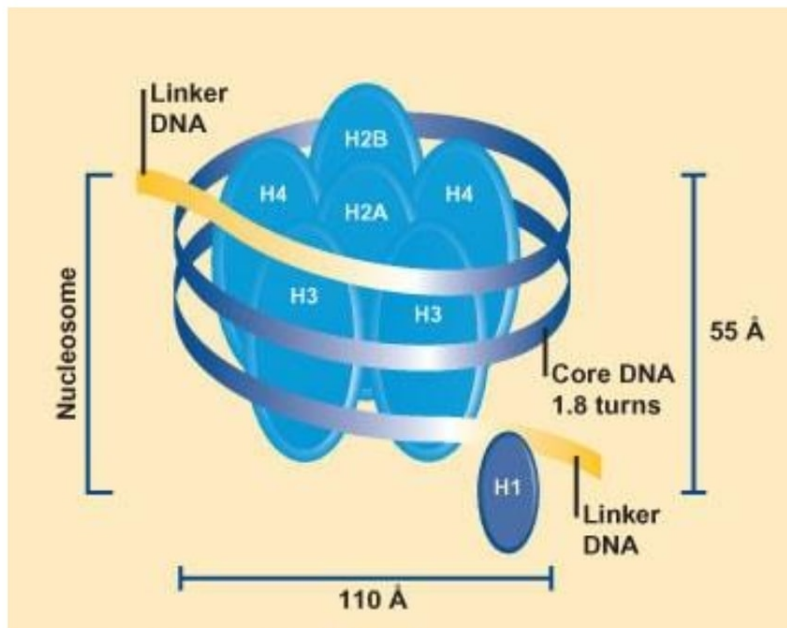


Figure 5.1: The nuclear DNA is organized within a nucleosomal structure, where approximately 146 base pairs of DNA are wrapped around a histone octamer composed of two copies each of H2A, H2B, H3, and H4 proteins. Variants of histones, including H2AX, can also be present in the nucleosomes [35].

When a DSB occours, the H2AX protein gets phosphorylated by a kinase (DNA-PK, ATM, ATR) via the addition of a phosphate group ($PO_4^{3-}$) to the polar side chain of the amino acid.
Within one minute from the occouring of the DSB, 50% of H2AX histones that will be involved in the whole process result already phosphorylated, and within 10 minutes from the beginning the maximum number of $\gamma$-H2AX is reached. The phosphorylation of this histone represents the first step in the localization of damage and the recruitment of the DNA repair protein complex, making it a key step in the DNA Damage Response (DDR):

- it acts as an epigenetic signal for recognition, triggering the repair mechanism;

- it reduces chromatin density, facilitating the insertion of protein complexes for repair;

- it modulates DNA damage checkpoints, halting or slowing down the cell cycle for the necessary time for the process.[35–38]

### 5.1.2 53BP1

The protein 1 that binds to the tumor suppressor P53, known as 53BP1, is composed of 1972 amino acids and its structure makes it one of the main mediators of DSB signaling, as it presents surface interaction sites for numerous proteins involved in DSB repair pathways. 53BP1 plays a crucial role in coordinating and regulating the repair of DSBs by the non-homologous end joining (NHEJ) pathway, which is one of the major DNA repair mechanisms in cells. It acts as a scaffold protein that helps recruit other repair factors to the site of DNA damage, facilitating the repair process. Moreover, this protein inhibits the homologous recombination repair pathway by antagonizing the binding of another key repair protein, BRCA1, to the damaged DNA. This suppression is important for maintaining the balance between NHEJ and HR repair pathways (Fig. 5.2).
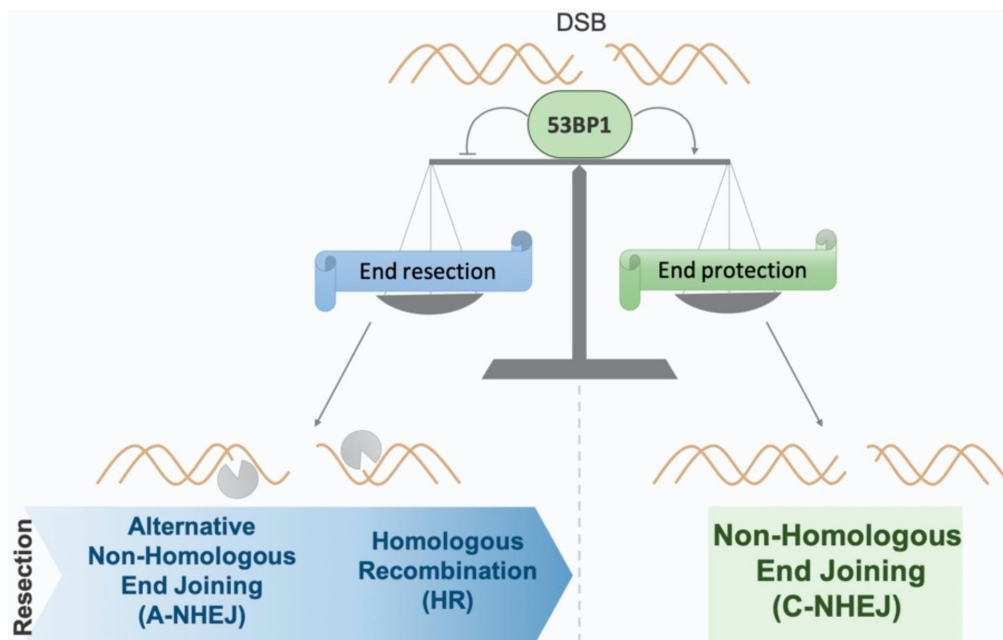


Figure 5.2: The importance of 53BP1 in the choice of double-strand break repair pathway. 53BP1 plays a pivotal role in the balance of the DSB repair choice by limiting DSB end resection, thus promoting canonical non-homologous end joining (C-NHEJ) over homologous recombination (HR) and the mutagenic alternative NHEJ (A-NHEJ), which both require a first resection step [39].

As mentioned above, the identification of DSB sites through the accumulation points of repair proteins (*foci*), and the study of DSB repair dynamics using the $\gamma$-H2AX *foci* assay, constitute an extremely useful tool in the clinical setting. They offer the opportunity to monitor the cellular response to a particular treatment, providing insights into the effectiveness of radiotherapy and chemotherapy on tumor cells while evaluating potential side effects on healthy tissues.

In this analysis, the assay is based on the localization and quantification of *foci* using antibodies specific to the $\gamma$-H2AX histone. As described in the previous paragraph, the formation of $\gamma$-H2AX *foci* in proximity to the break site represents the initial step in the DSB repair mechanism, making them excellent biomarkers for radiation-induced damage. A secondary antibody, labeled with a fluorophore specific to the primary antibody, is used for indirect immunofluorescence, responsible for the fluorescent signal. Under a fluorescence microscope, $\gamma$-H2AX *foci* appear as punctate signals characterized by different intensity and size.

Actually, many experiments conducted in the last decade have demonstrated that while the formation

of a DSB always involves the phosphorylation of the H2AX histone, the presence of $\gamma$-H2AX *foci* cannot always be considered a biomarker for DNA double-strand breaks. As a matter of fact, $\gamma$-H2AX is involved in many other processes associated with chromatin structure modifications that may not necessarily involve DSBs. Therefore, although the correlation between $\gamma$-H2AX *foci* and DSBs is strong, the multifunctionality of the $\gamma$-H2AX protein introduces the risk of overestimating the actual number of DSBs due to the possibility of nonspecific signals and false positives [40–44].

To minimize this problem, a colocalization approach can be utilized, which consists in using different antibodies specific to other proteins involved in DDR together with $\gamma$-H2AX. By visualizing the results related to these different proteins in separate channels (with different fluorophores), a superposition can be made to reduce the number of false positives. The probability of nonspecific signals (not related to a DSB) for both $\gamma$-H2AX and other DDR proteins in the same DNA region is low. The most commonly used target for colocalization in the *foci* assay is the 53BP1 protein. Similar to $\gamma$-H2AX, 53BP1 accumulates in an oligomerized form at the DSB site, leading to the formation of 53BP1 *foci*. The choice of 53BP1 is supported by experimental results, including the similarity between the kinetics of 53BP1 *foci* and $\gamma$-H2AX *foci* and the genetic distinction between the roles of the two proteins in the repair mechanism.[45, 46].

Fig. 5.3 shows three different captures of the same cell sample, in order to see nuclei, $\gamma$-H2AX *foci* and 53BP1 *foci*.
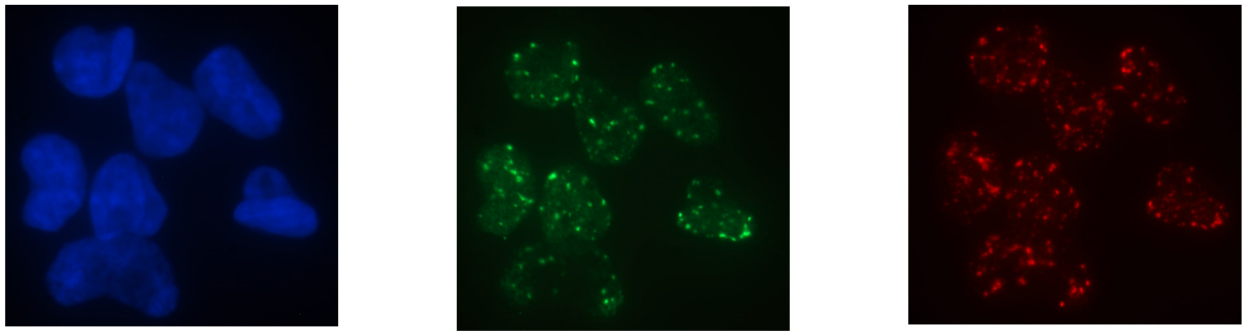


Figure 5.3: From left to right: fluorescence of the nuclei, of $\gamma$-H2AX and of 53BP1.

## 5.2 The *foci* assay procedure

As mentioned, the indirect immunofluorescence technique was utilized to visualize the *foci*. This technique involves a series of steps to prepare the cellular samples for analysis, specifically consisting of *rattus norvegicus* osteosarcoma cells (UMR106 cell line). Prior to the analysis, these cells were located into plastic containers called Petri dishes (d = 35 mm, h = 10 mm), shown in Fig. 5.4:



Figure 5.4: On the left, of the Petri dishes used for the experiment [47]. On the right, picture of the Petri dishes labelled with the dose of irradiation; the ones unlabelled are not irradiated and used as "control" samples.

### 5.2.1 Irradiation

At the L.E.N.A. of Pavia, UMR106 cell cultures were irradiated with various doses of photons from $^{60}$Co. 8 Petri dishes containing the cells in adhesion were labelled and lowered with a pulley (Fig. 5.5) inside a dedicated well surrounded by 13 cobalt bars.



Figure 5.5: Picture of the pulley used to place the Petri dishes containing the cells in proximity of the cobalt source.

The photons used for irradiation are those generated from the decay of $^{60}$Co, which has an half-life of 5.3 years, and decays into $^{60}$Ni by emitting two principal photons with energies of 1.1732 MeV and 1.3325 MeV. In order to expose the cells to two different dose values, they were irradiated with different periods of time. The irradiation times, respectively 30 seconds to achieve a dose of 0.5 Gy and 90 seconds to reach a dose of 2 Gy, are calculated using a previously established calibration method, assuming electronic equilibrium within the cells.
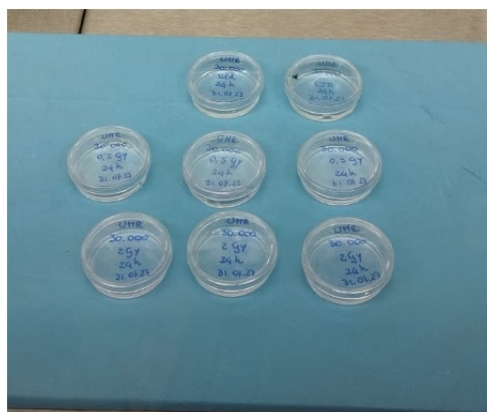


Figure 5.6: Picture of the Petri dishes lowered with the pulley.

### 5.2.2 Hybridization

First, the slides containing the cellular samples were subjected to a process called hybridization, in which specific antibodies targeting the $\gamma$-H2AX and 53BP1 proteins were applied to the samples. To enable their visualization, the antibodies were conjugated with fluorescent probes called fluorophores, able to emit fluorescent signals when excited by specific wavelengths of light. The $\gamma$-H2AX-specific antibodies were labeled with one type of fluorophore, while the 53BP1-specific antibodies were labeled with a different one, so that the two types of *foci* can be distinguished and observed separately. The prepared samples were then examined using a fluorescence microscope. The microscope (Fig. 5.7)
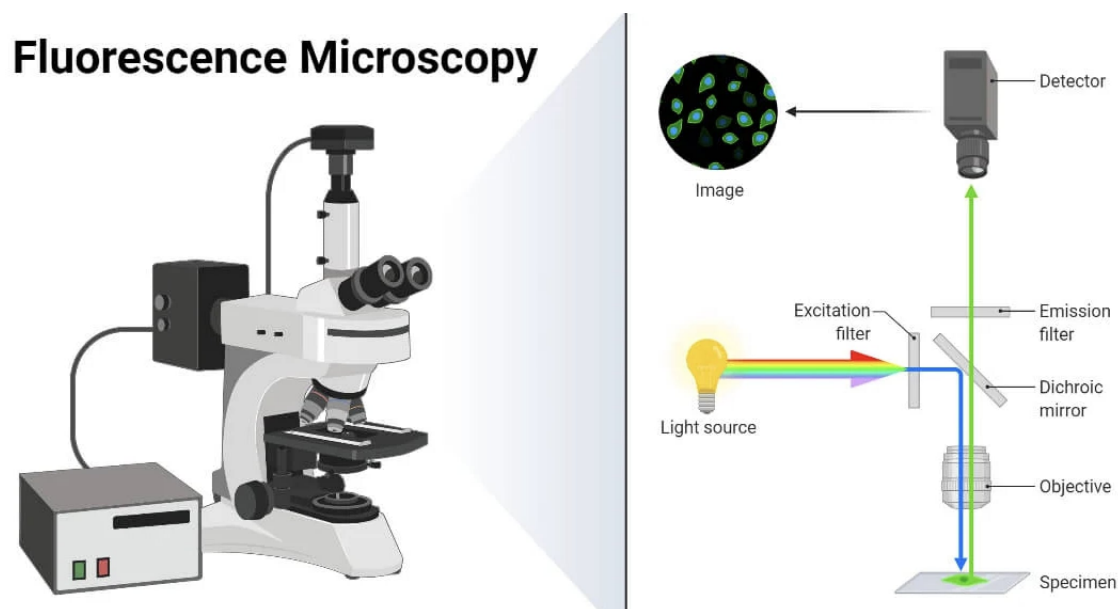


Figure 5.7: On the left, representation of a fluorescence microscope. On the right, the scheme of the working principle of a fluorescent microscope.

emits light of the appropriate wavelength, selected through an excitation filter, to excite the fluorescent probes attached to the antibodies. When excited, the probes emit fluorescent signals that can be detected and visualized through the microscope. The emitted radiation is then filtered by an emission filter, ensuring that only the fluorescent light emitted by the sample reaches the eyepiece, separating it from the excitation radiation [48]. The hybridization process is a crucial step in optimizing the analysis system, as it directly impacts the quality of the images that will be analyzed. Poor hybridization can result in increased background fluorescence, which can affect the accuracy of the analysis. To ensure optimal results, a protocol was developed at the Laboratory of Radiation Biophysics, following established guidelines from the scientific literature. The hybridization protocol involves several phases.

**Permeabilization** To prepare the samples for antibody penetration, this step was performed at two time points: 30 minutes and 24 hours after irradiation. The samples were initially treated with a 4% paraformaldehyde solution to prevent decomposition and maintain the integrity of cellular components through fixation. Subsequently, they were stored in phosphate-buffered saline (PBS). After removing the PBS from the Petri dishes, a permeabilization buffer (PB) was added to each sample in a volume of 1 mL. The PB solution consisted of 0.25% of Triton X-100 which, being a detergent, induces structural modifications in the cell membrane, rendering it permeable to the subsequent introduction of antibodies. Once the PB was added, it was allowed to act at room temperature for 15 minutes, facilitating the permeabilization process. Following this incubation period, the PB was carefully removed, and the cells were washed with PBS, using approximately 1.5 mL of PBS per sample. This washing step aimed to eliminate any residual PB and ensure the samples were ready for the subsequent stages of the experiment.
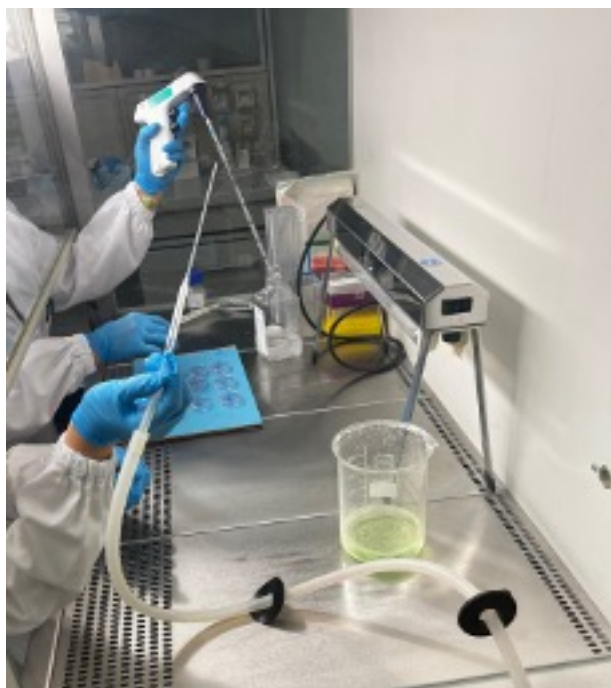
Figure 5.8: Picture of the performing of first step of the process.

**Blocking**   To create the blocking buffer (BB), a solution is made using PBS containing 10% goat serum, 1% bovine serum albumin (BSA), 0.1% Tween 20, and a concentration of 0.3 M glycine. The purpose of adding goat serum is to prevent the primary antibodies from binding to non-specific Fc receptors. BSA is included to occupy any non-specific binding sites, enhancing the binding specificity of the antibodies to the desired antigens and reducing background interference in the resulting images. Tween 20 is used to block any remaining non-specific binding sites. Glycine is important as it helps deactivate any unreacted aldehydes during fixation, minimizing the presence of background fluorescence. Once the BB is prepared and filtered, the original PBS solution is removed from the sample flasks and replaced with 1 mL of the blocking buffer. The samples are then left to incubate at a temperature of 37°C for one hour.

**Addition of primary antibodies**   First, the BB is removed and replaced with 1 mL of solution containing primary antibodies of two types: Anti $\gamma$-H2AX and Anti 53BP1. The Anti $\gamma$-H2AX is a specific antibody that binds to a particular amino acid sequence (from 134 to 142) of the $\gamma$-H2AX histone. On the other hand, the Anti 53BP1 is an antibody that recognizes a specific region (amino acids 350 to 400) of the 53BP1 protein. These antibodies are added to the solution to target and bind to their respective antigens. Before adding the primary antibody solution to the samples, the antibodies should be briefly centrifuged. This step helps to remove any protein aggregates that may have formed during storage, as these aggregates could interfere with the staining process. After adding the primary antibody solution, the samples are incubated for 1 hour at 37°C (or overnight at 4°C) to allow sufficient time for the antibodies to bind to their targets. Once the incubation period is complete, the primary antibody solution is removed from the samples. To ensure proper washing and removal of unbound antibodies, four washes are performed on each sample. Each wash lasts for 5 minutes and is done using a washing buffer (WB). The washing buffer is made up of PBS with Triton X-100 at a concentration of 0.2%.

**Addition of secondary antibodies**    To continue with the staining process, the samples are now ready for the addition of secondary antibodies. This step must be carried out in low light conditions to prevent photobleaching, which is the degradation of fluorescent probes due to exposure to light. The WB is removed from the samples, and 1 mL of a secondary antibody solution is added to each sample. The secondary antibody solution consists of two different antibodies: Anti-mouse (for $\gamma$-H2AX) and Anti-rabbit (for 53BP1). These secondary antibodies are specific to the primary antibodies used in the previous step and will help amplify the signal. Fig. 5.9 shows the process for secondary antibody production.
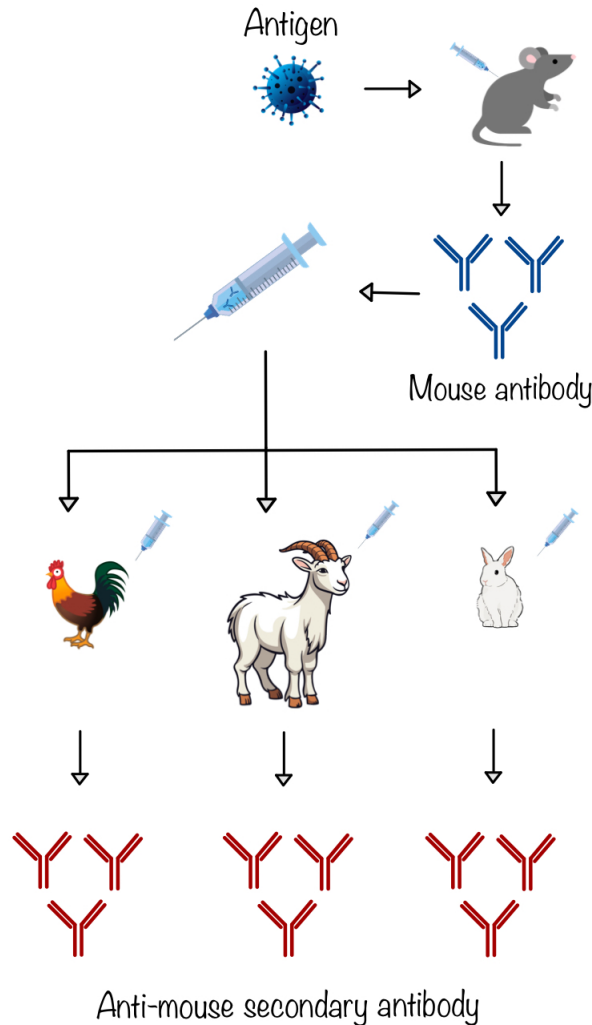


Figure 5.9: Scheme of primary and secondary antibodies production.

The samples are then kept in the dark for 1 hour at 37°C to allow the secondary antibodies to bind to the primary antibodies. After the incubation period, the secondary antibody solution is removed, and the samples undergo another round of washing. As before, four washes are performed on each sample, with each wash lasting 5 minutes. The same WB with PBS and Triton X-100 is used for these washes. By using secondary antibodies, the risk of non-specific binding is minimized, ensuring that the secondary antibodies only bind to their intended primary antibodies. This is crucial for obtaining accurate and specific results, especially when multiple primary antibodies are used simultaneously in immunofluorescence techniques. The primary antibodies were tagged with fluorescent probes known as Alexa Fluor 555 (AF555) and Alexa Fluor 488 (AF488) during the secondary antibody step. AF555 is specifically attached to the Anti-mouse secondary antibody, while AF488 is attached to the Anti-rabbit secondary antibody. These fluorophores emit fluorescence at different wavelengths when excited

by specific light sources (see Fig. 5.10). AF555 has an optimal excitation wavelength at 555 nm and emits fluorescence at 580 nm. This allows the visualization of the $\gamma$-H2AX *foci* as red signals under a microscope. AF488 has an optimal excitation wavelength at 488 nm and emits fluorescence at 525 nm. This allows the visualization of the 53BP1 *foci* as green signals under a microscope. These Alexa Fluor fluorochromes are chosen for their excellent solubility in water, tolerance to pH variations, and high quantum fluorescence yield, meaning they emit a high number of photons compared to the number of photons absorbed. Moreover, they are designed to minimize issues related to photobleaching and self-quenching, which can reduce the quality and intensity of the fluorescence.
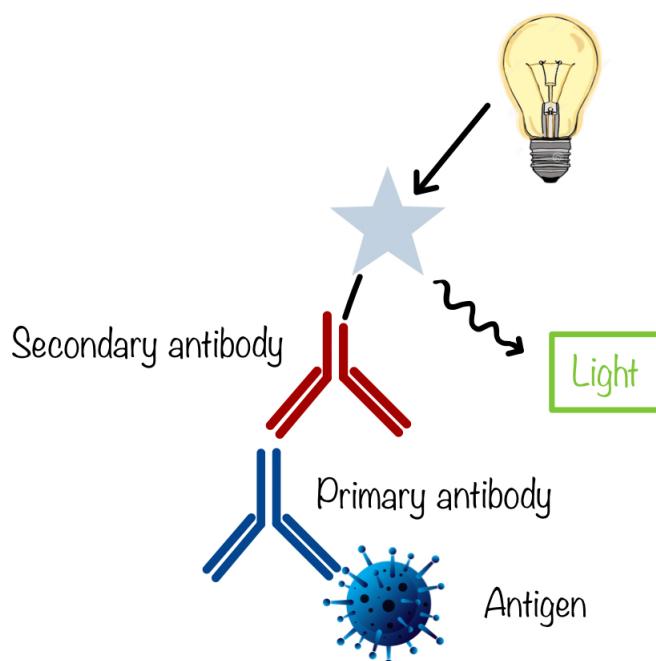


Figure 5.10: Schematic representation of the fluorochrome working principle.

**Post hybridization** To start, the WB is removed from the vials and 1.5 mL of PBS are added to each sample. Then, the PBS is removed and replaced with 2-3 drops of Prolong Gold antifade with DAPI. Next, each sample is covered with a cover slip measuring 18×50 mm. It is important to apply gentle pressure to ensure there are no air bubbles trapped underneath. The samples are then left to incubate overnight at room temperature in a dark environment. At this stage, the slides can be analyzed using a microscope or stored at -20°C for longer periods of time. The purpose of using Prolong Gold antifade is to prevent fading, which is the loss of fluorescence intensity over time. DAPI, on the other hand, is a fluorescent dye that can penetrate cell membranes and binds strongly to DNA regions rich in Adenine-Thymine sequences. When bound to the DNA, DAPI absorbs ultraviolet light at a wavelength of 358 nm and emits a blue light at a wavelength of 461 nm. This property allows DAPI to be used as a nonspecific stain for cellular nuclei. However, it requires an UV lamp as the light source for observation under a microscope [35].

The workstation utilized for the image acquisition is equipped with an Olympus BX51 fluorescence microscope (Fig. 5.11), a scanning stage capable of accommodating 8 slides, a high-resolution CCD Retiga-2000R camera using the 100x objective with oil immersion, a PC, and a monitor used to visualize the images.
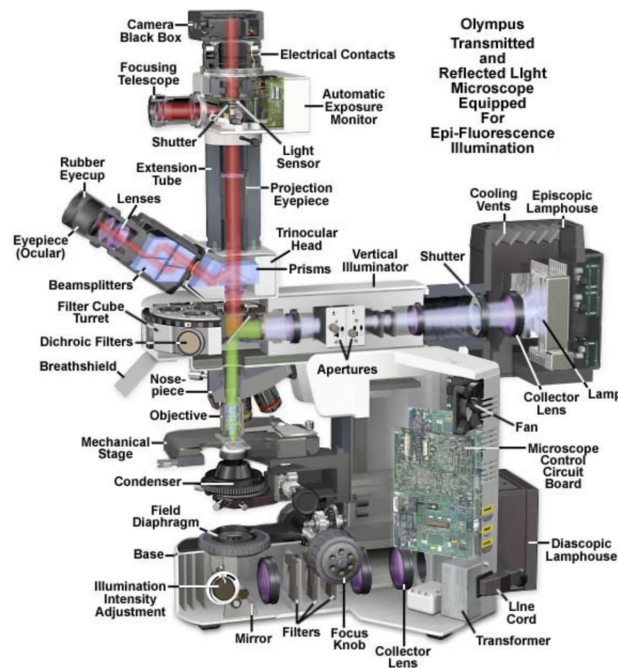
Figure 5.11: Scheme of all the components of the used microscope [49].

## 5.3 Data analysis

**ImageJ** ImageJ (see Fig. 5.12) is a powerful tool used for digital image processing. It was developed by the National Institutes of Health in the United States and released in the public domain. The program, based on the Java language, offers a wide range of functionalities and features to manipulate and analyze images.



Figure 5.12: ImageJ logo.

The software supports various image formats, including TIF, PNG, GIF, and JPEG, as well as some "raw" formats. It can work with grayscale images (8-bit, 16-bit, and 32-bit) and color images (8-bit and 24-bit). Additionally, ImageJ can handle image stacks, which are overlapping series of images that can be spatially or temporally related. This allows the user to analyze three-dimensional structures or time-dependent processes within a single interface. The program offers numerous tools for image analysis and processing. It is possible to measure pixel values and statistics within user-defined selections, such as regions of interest or segmented objects based on intensity thresholds. ImageJ also enables distance and angle measurements, creation of density histograms, and tracing of line profiles between specified points. Moreover, standard image processing operations like logical and arithmetic manipulations, contrast adjustments, Fourier analysis, smoothing, contour recognition, and median filtering can be performed. One of the most remarkable features of ImageJ is its ability to support multiple images simultaneously, limited only by the available computer memory. This allows users to analyze large datasets efficiently. The versatility and user-friendly development environment of ImageJ have made it widely used in various fields: it finds application in radiology for image processing tasks,

in the development of automated systems for hematology, and as a teaching tool for image processing education.

In this case, ImageJ was fundamental for the *foci* counting. Overall, the procedure used for each analyzed image follows:

- **Nuclei selection**: first of all, the image in which the DAPI fluorescence is displayed is opened in order to select all the visible nuclei in the picture (Fig. 5.13);
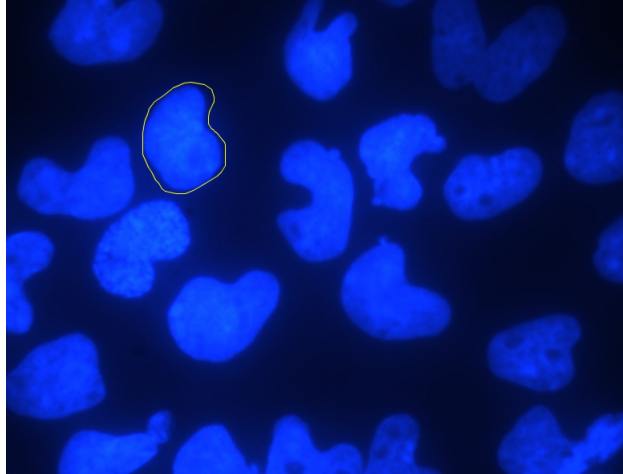


Figure 5.13: DAPI doped nuclei.

- **Area measuring**: due to the fact that UMR106 cells are highly variable in dimensions (see Fig. 5.14), the area of each of them is saved using the "Measure" function of the Region of Interest (ROI) manager of ImageJ;
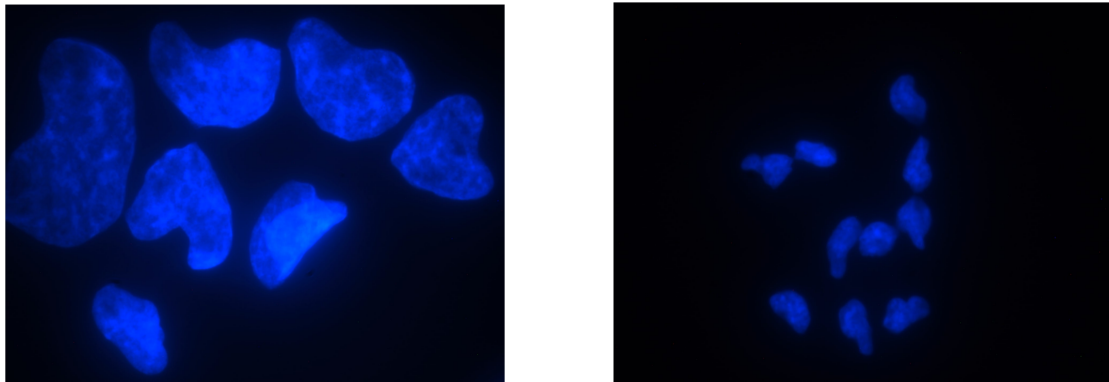


Figure 5.14: Comparison in size between cells of two pictures taken on the same slide.

- **γ-H2AX *foci* counting**: using the "Find Maxima" function of the tool, the *foci* are counted (Fig. 5.15).
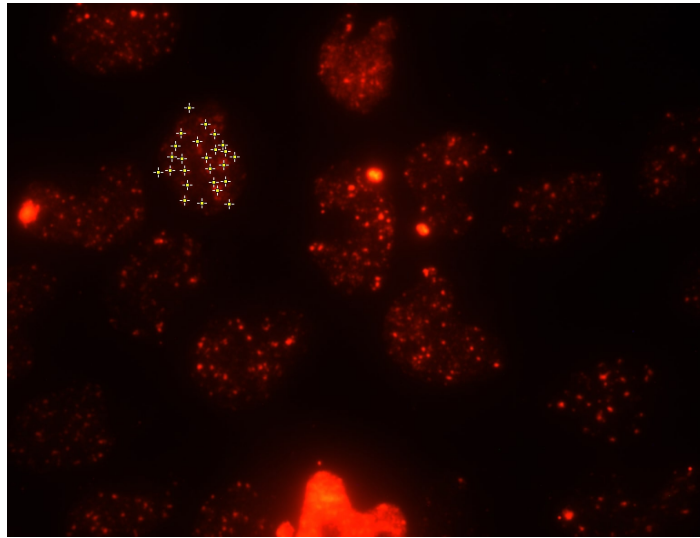


Figure 5.15: γ-H2AX protein's accumulation is clearly visible as red spots inside cells.

- **53BP1 *foci* counting**: as in the previous point, using the "Find Maxima" function of the tool, the *foci* are counted (Fig. 5.16).
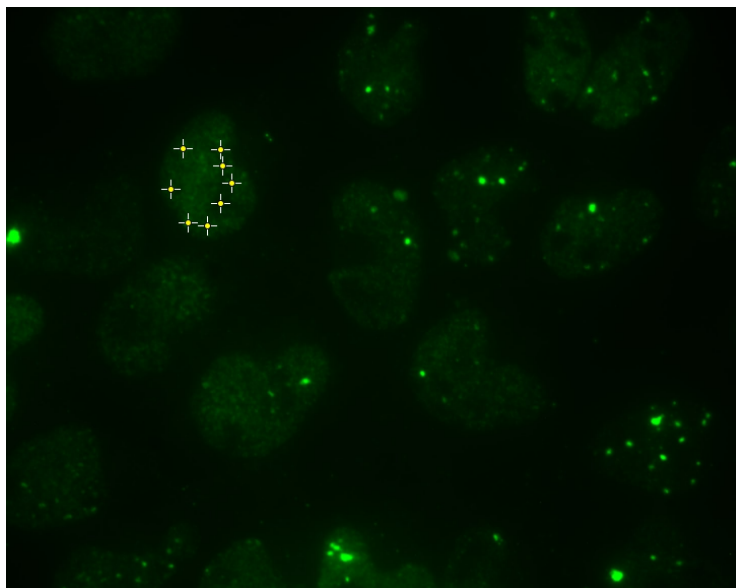


Figure 5.16: 53BP1 protein's accumulation is clearly visible as green spots inside cells.

**Analysis of the results** As mentioned, the samples were permeabilized at two different time points from the irradiation with the source of $^{60}$Co: after 30 minutes and after 24 hours. This strategic approach was employed to effectively capture and compare the cellular state at these precise moments in time. The initial permeabilization, occurred after 30-minute from the irradiation, is fundamental to obtain insights about the immediate effects of radiation exposure on the cells. This means that freezing the cells as soon as possible after the irradiation allows to have a window on the initial impact and assess the initial state of the cellular response to the radiation source.
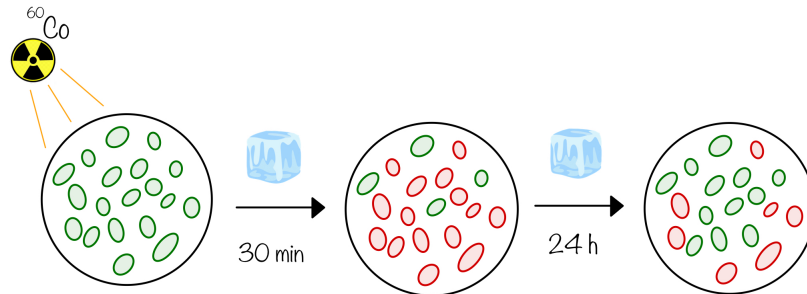


Figure 5.17: Schematic depiction of cellular repair mechanisms. Healthy cells within the Petri dish are illustrated in green, while the red cells indicate damage.

On the other hand, the second permeabilization point, which occurs after 24 hours, was chosen because it is a crucial indicator for evaluating the cells' ability to repair DNA damages occurred because of the irradiation (see Fig. 5.17). Totally, 4 different situation needed to be analyzed (Fig. 5.18):

- 2 Gy absorbed dose, freezing after 30 minutes;

- 2 Gy absorbed dose, freezing after 24 hours;

- 0.5 Gy absorbed dose, freezing after 30 minutes;

- 0.5 Gy absorbed dose, freezing after 24 hours.
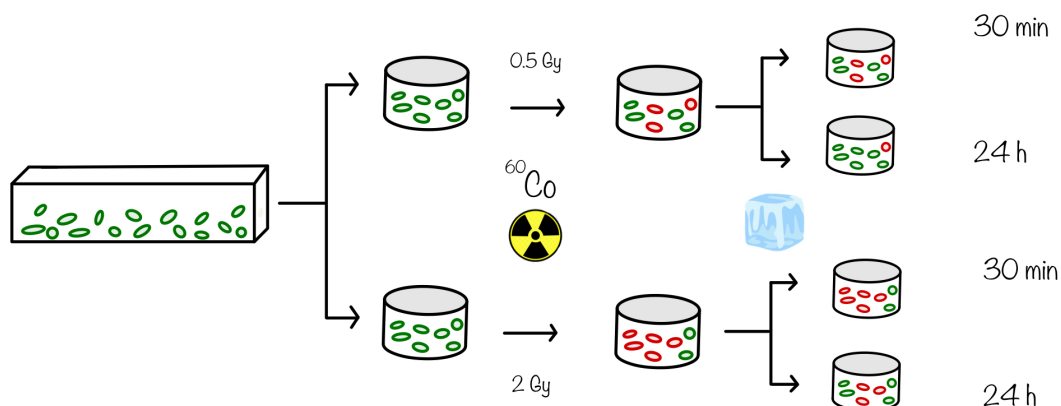


Figure 5.18: Schematic representation of all the cell situations analyzed.

For every scenario, three slides were examined under the microscope, and within each slide, three images were captured at distinct zones, in order to have a sufficient statistic for the following analy-

sis. For each taken image the maximum amount of distinguishable cells were analyzed with ImageJ following the procedure described before, in order to mediate the counted *foci* on a sufficiently large sample. Notably, the UMR106 cells, being of tumoral origin, exhibit significant variability in their dimensions, causing to a huge variation of the counts of *foci* across different cells. Another reason why a large sample was necessary is the difficulty in finding a universal threshold for all the samples, as some images presented challenges in removing background noise, contaminations or nuclei overlaps. The results are summarized in 5.1

Table 5.1: *Foci* counts with associated the mean uncertanty for each result.

| *Time* | **0.5 Gy** | **2 Gy** |
|---|---|---|
| *30 min* | $32.1 \pm 1.9$ | $50 \pm 12$ |
| *24 h* | $23.5 \pm 1.8$ | $16.3 \pm 3.0$ |

As expected, the number of *foci* found in cells blocked after 30 minutes is higher compared to the one found in cells freezed after 1 day, due to the damage repair process. Additionally, it is worth noting the substantial uncertainties associated to the *foci* counts in the 2 Gy cells (see Fig. 5.19): this is due to the fact that these samples were highly damaged, making it very complicated for the operator to count the points of damage, thus leading to a high variability of the counts from one cell to another. Finally, another unexpected result concerns the fact that the counts after 1 day with 05 Gy cells are higher compared to the damages found in 2 Gy cells: this is probably due to the fact that the threshold chosen for 2 Gy cells was too high for the sample at 24 hours. Indeed, setting the threshold too low for samples taken at 30 minutes resulted in an excessive count of damage instances, while an excessively high threshold led to an underestimation of the counts for the 24-hour samples.
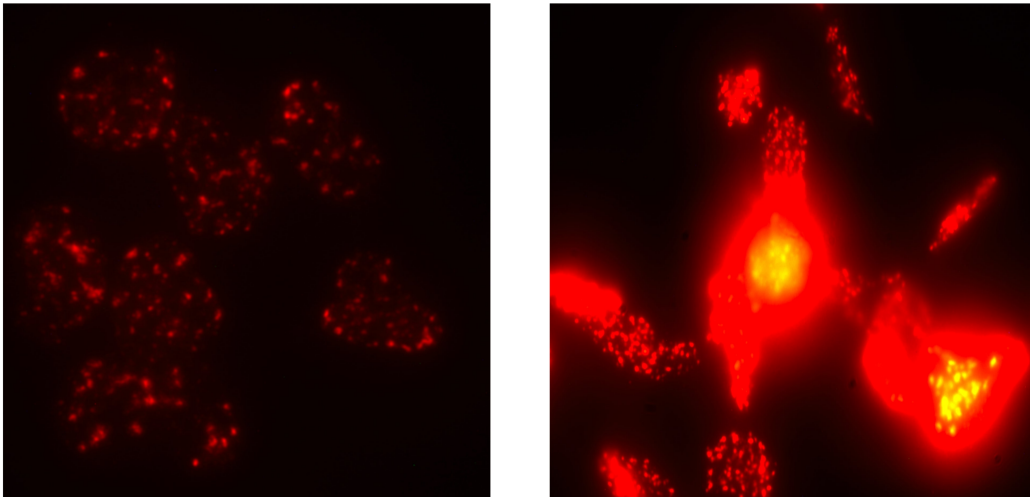


Figure 5.19: Example of cells blocked after 30 minutes: on the left side, cells irradiated with 0.5 Gy; on the right side, cells irradiated with 2 Gy.

## 5.4 Comparison with simulations

Simulations were run with with the human fibroblast as target and a $^{60}$Co source distributed with a planar geometry near the cell. In order to understand how many events were needed to simulate the two doses obtained in the experimental application, namely 0.5 Gy and 2 Gy, different number of events were launched, plotted and then fitted with a linear regression to find the parameters needed. The results are shown in Fig. 5.20:
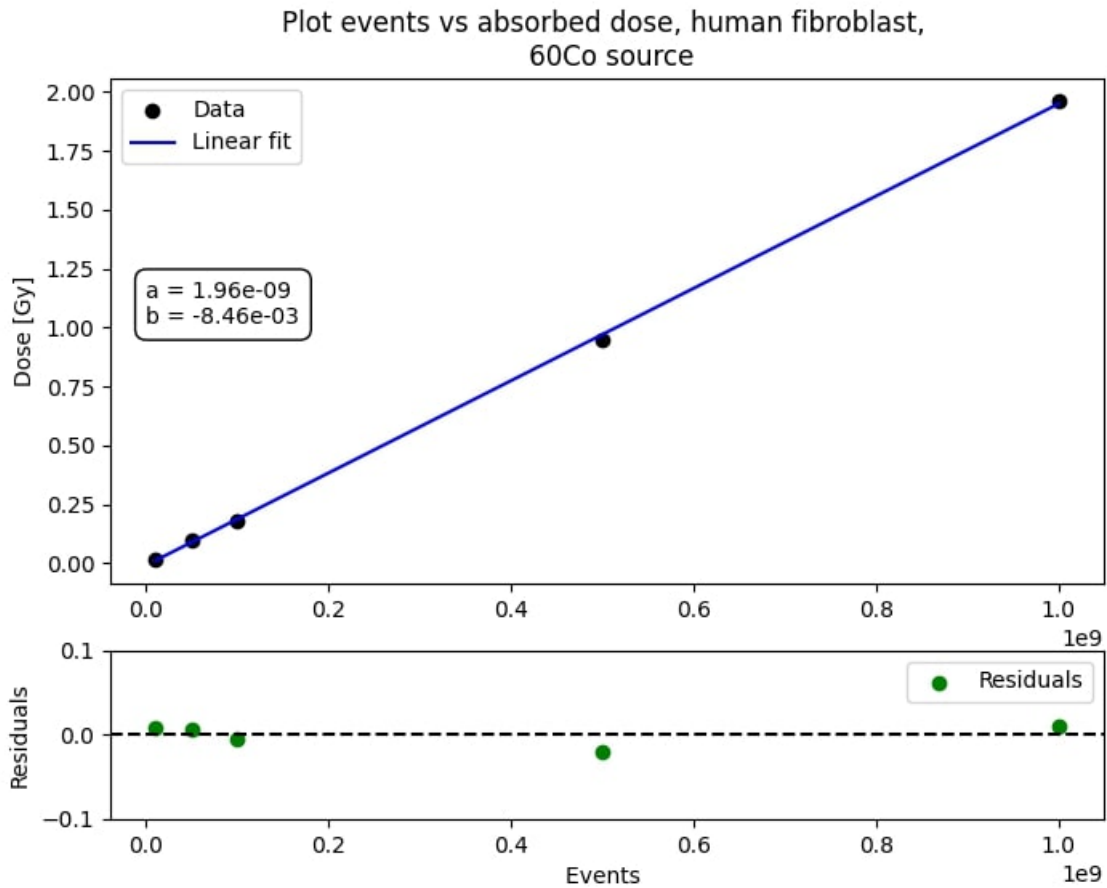


Figure 5.20: Plot of linear regression and of residuals performed on simulations with a source of $^{60}$Co.

Once the runs of the two simulations were completed, the damage yields were inserted in the repair python macro provided inside the molecularDNA example. This program, based on the theoretical model proposed by [5] (see Appendix), is designed to simulate the damage repair process happening within the cell during the initial 25 hours following irradiation. The obtained results are shown in Fig. 5.21 and Fig. 5.22:
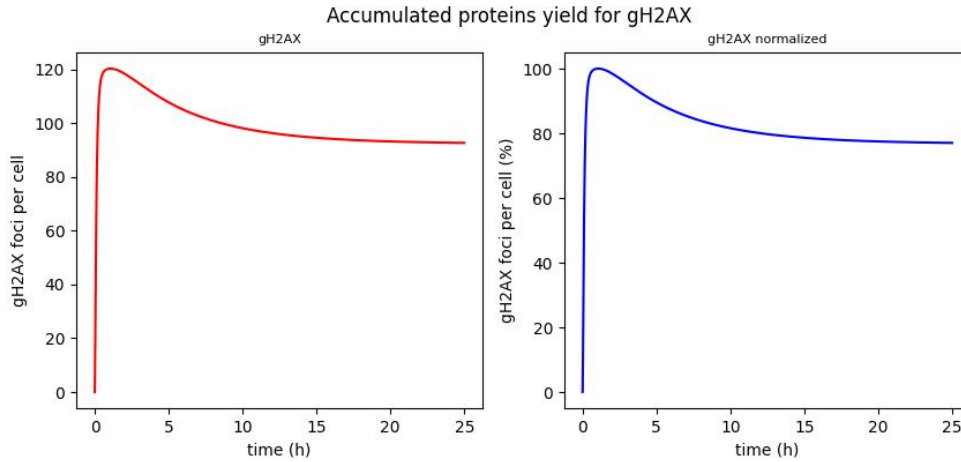


Figure 5.21: Proteins yield from 0 to 24 h after irradiation of 0.5 Gy. On the right side, normalization of the graph on the left.
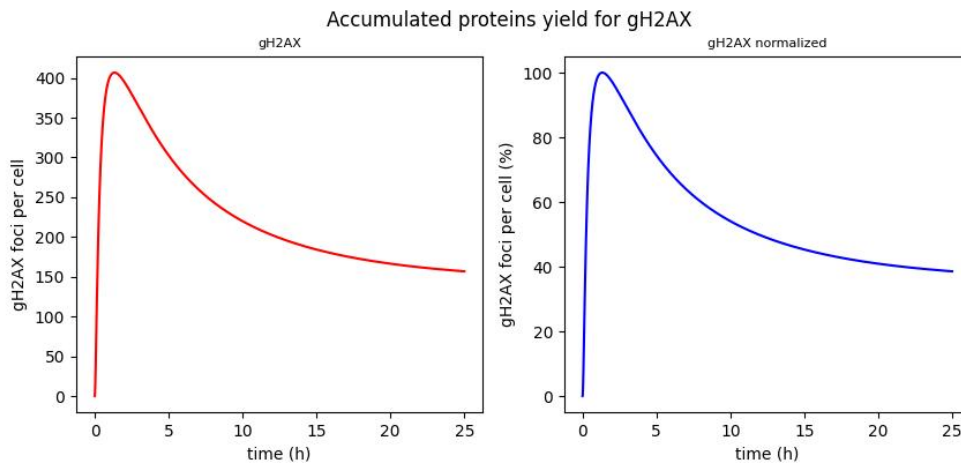


Figure 5.22: Proteins yield from 0 to 24 h after irradiation of 2 Gy. On the right side, normalization of the graph on the left.

As expected, the number of *foci* estimated for the 2 Gy dose are higher compared to the one computed for the 0.5 Gy dose, but the results are not compatible with the experimental data.

As a matter of fact, by comparing the experimental results with the simulated ones it is evident that the latter are an overestimation of the *foci* number counted on the images. To correct this systematic error, by setting on the hypothesis that the $\gamma$-H2AX protein is indicator only of DSBs (as explained before, it is not always true), the curves were re-normalized on the maximum number of DSBs found at the end of the simulations.
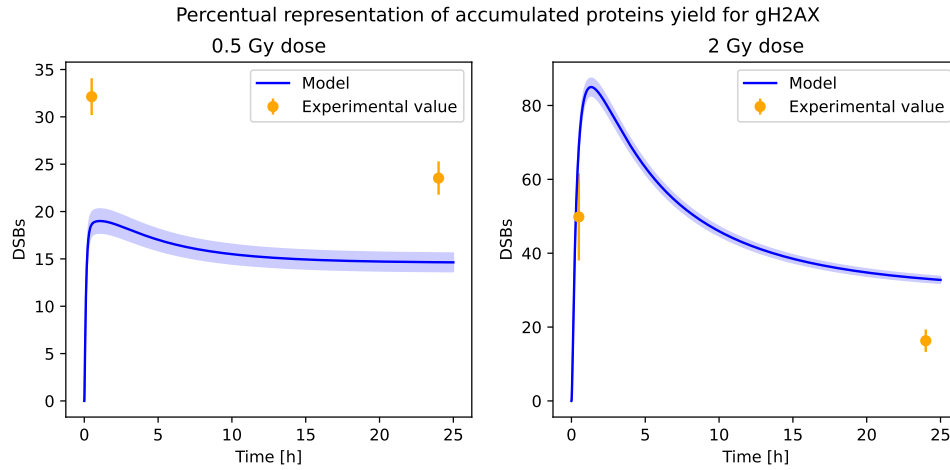


Figure 5.23: Comparison between experimental data and normalized simulation. The error bar associated to the points derives from the uncertainty associated to the mean of the *foci* counting, while the one on the simulation is a 4% deriving from the studies conducted on the stability of the simulation (Tab. 4.2) and Tab. 4.1).

As shown in Fig. 5.23, the simulation with 0.5 Gy dose lead to a lower esteem of the maximum number of *foci* compared to the experimental findings, while the simulation with a 2 Gy dose still yielded a higher count of DSBs. Since the experimental results are semi-quantitative, due to their sensitivity to the threshold chosen by the operator for the *foci* counting, they were adapted to the simulation by finding the scale parameter that maximizes the compatibility between the curve and the points. The final graph obtained is shown in Fig. 5.24:
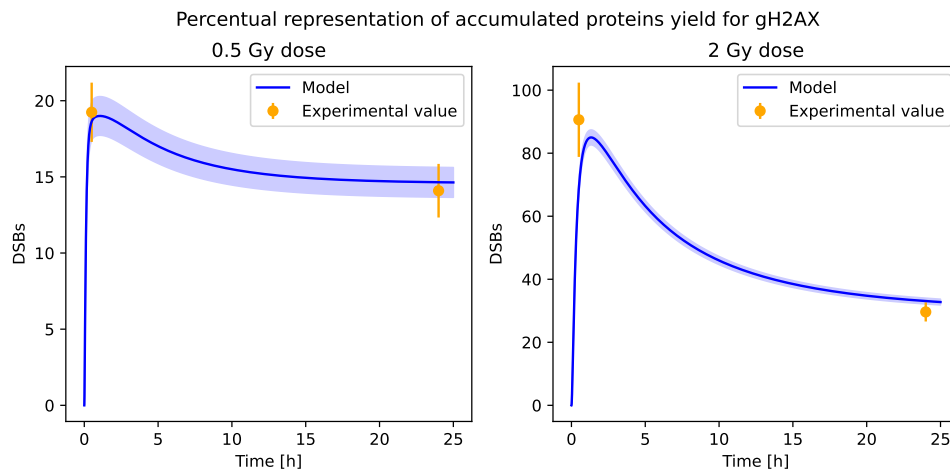


Figure 5.24: Comparison between the re-scaling of the experimental data and normalized simulation. The error bar associated to the points derives from the uncertainty associated to the mean of the *foci* counting, while the one on the simulation is a 4% deriving from the studies conducted on the stability of the simulation (metti ref).

Concerning the 0.5 Gy dose, the overall pattern of the repair model aligns well with the two experimental points within the margin of error. On the other hand, in the case of samples exposed to 2 Gy, the curve lies between the two data points, leading to an underestimation of the first point and an overestimation of the second one. It is plausible that this mismatch is linked to the aforementioned constraints associated with *foci* counting in the context of cells exposed to the 2 Gy dose.

# Conclusions

The driving force behind the thesis' analysis was the use of the GEANT4-DNA simulation toolkit, an innovative resource that helped to comprehensively analyze and predict the effects of radiation on cells' DNA. First of all, the stability of the outputs was analyzed, finding a threshold in the necessary statistics that was a great compromise between computing time and reliability of the results. Subsequently, predictions concerning $^{111}$Ag radiation-induced damage were extrapolated through a secondary set of simulations, revealing that DNA damage yields were higher when the radiation source was distributed superficially rather than internalized in the cell's volume. Finally, the last objective was comparing simulations with an actual *foci* assay experiment conducted in Pavia. At the L.E.N.A., UMR106 cells were irradiated with 2 different doses, 0.5 Gy and 2 Gy. Following the simulation of cell damages, the Belov model [5] was applied to emulate the repair process, permitting a side-by-side evaluation with *foci* counts at two discrete time points: 30 min and 24 hours from the irradiation. The obtained curve was aligned with the experimental counts by considering the difficulties in counting the actual points of damage in cells, confirming that the predicted trend was followed by the experimental data within an acceptable margin of error.

The outcomes derived from this study carry a profound significance. Specifically, the computed S-values, quantifying the potential harm inflicted on DNA by radiation exposure, hold a fundamental role since they serve as a bridge between simulated predictions and experimental applications. As a matter of fact, the obtained results will be crucial since they can be used to develop models that will be applied to *in vitro* studies, such as *foci* assays and cell survivals in 2D cultures or 3D organoids, involving the innovative radionuclide $^{111}$Ag.

# Appendix

The following chapter has the objective of providing more details about the repair model proposed by Belov [5].

A mass-action chemical kinetics approach is adopted in order to simulate DNA lesion processing by pathway-specific enzymes, and model kinetic parameters are calibrated by fitting calculated curves to experimental data (Tab. A.1).

**NHEJ model**   The dynamic alteration in the levels of NHEJ intermediate complexes and $\gamma$-H2AX foci is represented by the following system of ordinary differential equations:

$$\frac{dn_0}{d\tau} = \alpha(L)\frac{dD}{dt}N_{ir} - n_0\left(k_1 x_1 + p_1 y_1\right) + k_{-1}x_2 + p_{-1}y_2$$

$$\frac{dx_2}{d\tau} = k_1 N_0 x_1 - x_2\left(k_{-1} + k_2 x_3\right) + k_{-2}x_4$$

$$\frac{dx_4}{d\tau} = k_2 x_2 x_3 - x_4\left(k_3 + k_{-2}\right)$$

$$\frac{dx_5}{d\tau} = k_3 x_4 - k_4 x_5^2 + k_{-4}x_6$$

$$\frac{dx_6}{d\tau} = k_4 x_5^2 - x_6\left(k_{-4} + k_5 x_7\right) + k_{-5}x_8$$

$$\frac{dx_8}{d\tau} = k_{-6}x_{10} + k_5 x_6 x_7 - x_8\left(k_{-5} + k_6 x_9\right) \tag{5.1}$$

$$\frac{dx_{10}}{d\tau} = k_{-7}x_{12} + k_6 x_8 x_9 - x_{10}\left(k_{-6} + k_7 x_{11}\right)$$

$$\frac{dx_{12}}{d\tau} = k_7 x_{10} x_{11} - x_{12}\left(k_8 + k_{-7}\right)$$

$$\frac{dx_{13}}{d\tau} = k_8 x_{12} + p_{12}y_{14} + p_{11}y_{15} + q_6 z_8 + r_8 w_5$$

$$\frac{dx_{14}}{d\tau} = \frac{k_9\left(x_5 + x_6 + x_8 + x_{10} + x_{12} + y_5\right)\times x_{15}}{k_{10} + x_5 + x_6 + x_8 + x_{10} + x_{12} + y_5} - k_{11}x_{13} - k_{12}x_{14}$$

Where

- $n_0$ is the scaled number of radiation-induced DBSs;

- $N_{ir}$ is the non-dimensional share of irreparable DSBs;

- $x_1$, $x_3$, $x_7$, $x_9$, and $x_{11}$ are scaled intracellular concentrations of the Ku, DNA-PKcs, LigIV=XRCC4=XLF, PNK, and Pol enzymes respectively;

- $x_2$, $x_4$, $x_5$, $x_6$, $x_8$, $x_{10}$, $x_{12}$, $x_{13}$, $x_{14}$, $x_{15}$, $y_5$, $y_{15}$, $z_8$, and $w_5$ are normalized intracellular concentrations of intermediate complexes; $\gamma$-H2AX foci, histone variant H2AX and some intermediate complexes which contribute to the fluorescent signal with the measurements of $\gamma$-H2AX foci induction;

- $k_i$ are scaled rate constants.

The initial conditions of this system for wild type cells are listed below: $n_0(0) = \alpha(L)D$, $x_2(0) = x_4(0) = x_5(0) = x_6(0) = x_8(0) = x_{10}(0) = x_{12}(0) = x_{13}(0) = x_{14}(0) = 0$. The variables $x_1$, $x_3$, $x_7$, $x_9$, $x_{11}$, and $x_{15}$ are set to be constant and equal to $x_1$.

The variables of the model are normalized per Ku total cellular level : $n_0 = N_0/X_1$, $x_i = X_i/X_1$, $y_5 = Y_5/X_1$; $z_8 = Z_8/X_1$; and $w_5 = W_5/X_1$. In terms of molar concentration, this level was estimated as $X_1 = N/(NA \cdot V_{\text{nucl}}) = 9.19 \times 10^{-7}$ M, where $N = 400000$ is the number of Ku molecules per cell, $NA$ is the Avogadro constant, $V_{\text{nucl}} = 7.23 \times 10^{-13}$ L is the average volume of the cell nucleus in human fibroblasts. Finally, $x_1 = 1$. Concerning kinetic parameters, we have

$k_1 = \frac{K_1 X_1}{K_8}$, $\quad k_2 = \frac{K_2 X_1}{K_8}$, $\quad k_3 = \frac{K_3}{K_8}$, $k_4 = \frac{K_4 X_1}{K_8}$, $\quad k_5 = \frac{K_5 X_1}{K_8}$, $\quad k_6 = \frac{K_6 X_1}{K_8}$, $k_7 = \frac{K_7 X_1}{K_8}$,

$k_8 = \frac{K_8}{K_8} = 1$, $\quad k_9 = \frac{K_9}{K_8}$, $k_{10} = \frac{K_{10}}{X_1}$, $\quad k_{11} = \frac{K_{11}}{K_8}$, $\quad k_{12} = \frac{K_{12}}{K_8}$,

$\frac{dx_2}{d\tau} = k_1 N_0 x_1 x_2 (k_1 + k_2 x_3) + k_2 x_4$, $\quad \frac{dx_4}{d\tau} = k_2 x_2 x_3 x_4 (k_3 + k_2)$,

$\frac{dx_5}{d\tau} = k_3 x_4 - k_4 x_5^2 + k_4 x_6$, $\quad \frac{dx_6}{d\tau} = k_4 x_5^2 x_6 (k_4 + k_5 x_7) + k_5 x_8$,

$\frac{dx_8}{d\tau} = k_6 x_{10} + k_5 x_6 x_7 x_8 (k_5 + k_6 x_9)$,

$\frac{dx_{10}}{d\tau} = k_7 x_{12} + k_6 x_8 x_9 x_{10} (k_6 + k_7 x_{11})$,

$\frac{dx_{12}}{d\tau} = k_7 x_{10} x_{11} x_{12} (k_8 + k_7)$.

$K_8$ is the rate that governs the final NHEJ process, unwinding repair elements. It is chosen as a scaling factor because its independence from different pathways competition is assumed.

**HR model**   The HR intermediate complexes behave as described by the following system of ordinary differential equations:

$$\frac{dy_2}{d\tau} = p_1 n_0 y_1 - y_2 (p_{-1} + p_3 y_4) + y_5 (p_4 + p_{-3})$$

$$\frac{dy_4}{d\tau} = p_2 y_3 - p_3 y_2 y_4 + y_5 (p_4 + p_{-3})$$

$$\frac{dy_5}{d\tau} = p_3 y_2 y_4 - y_5 (p_4 + p_{-3}) + r_{-1} w_2$$

$$\frac{dy_6}{d\tau} = p_4 y_5 - y_6 (p_5 y_7 + r_1 w_1) + p_{-5} y_8$$

$$\frac{dy_8}{d\tau} = p_{-6} y_{10} + p_5 y_6 y_7 - y_8 (p_{-5} + p_6 y_9 + q_1 z_1)$$

$$\frac{dy_{10}}{d\tau} = p_6 y_8 y_9 - y_{10} (p_7 + p_{-6})$$

$$\frac{dy_{11}}{d\tau} = p_7 y_{10} - p_8 y_{11} y_{12} + p_{-8} y_{13}$$

$$\frac{dy_{13}}{d\tau} = p_8 y_{11} y_{12} - y_{13} (p_9 + p_{-8})$$

$$\frac{dy_{14}}{d\tau} = p_9 y_{13} - y_{14} (p_{10} + p_{12})$$

$$\frac{dy_{15}}{d\tau} = p_{10} y_{14} - p_{11} y_{15}.$$

(5.2)

Where

- the initial conditions of this system for wild-type cells are set to $y_2(0) = y_4(0) = y_5(0) = y_6(0) = y_8(0) = y_{10}(0) = y_{11}(0) = y_{13}(0) = y_{14}(0) = y_{15}(0) = 0$;

- $y_1, y_3, y_7, y_9$, and $y_{12}$ variables are set to be constant and equal to $x_1$;

- $y_1, y_3, y_4, y_7,$ $y_9,$ $y_2, y_5, y_6, y_8, y_{10}, y_{11}, y_{13}, y_{14}$, and $y_{15}$ are scaled intracellular concentrations of intermediate complexes;

- $y_{12}$ is the normalized level of incoming homologous sequence $[\text{DNA}_{\text{inc}}]$;

- $p_i$ are scaled rate constants.

All the variables are normalized on the Ku total cellular level as $y_i = Y_i/X_1$. Moreover, the scaled reaction rates are $p_1 = P_1 X_1/K_8, p_{-1} = P_{-1}/K_8, \quad p_2 = P_2/K_8, \quad p_3 = P_3 X_1/K_8, \quad p_{-3} = P_{-3}/K_8, \quad p_4 = P_4/K_8, p_5 = P_5 X_1/K_8, p_{-5} = P_{-5}/K_8, p_6 = P_6 X_1/K_8, p_{-6} = P_{-6}/K_8, p_7 = P_7/K_8, \quad p_8 = P_8 X_1/K_8, \quad p_{-8} = P_{-8}/K_8, \quad p_9 = X_1/K_8, \quad p_{10} = P_{10}/K_8, \ p_{11} = P_{11}/K_8,$ and $p_{12} = P_{12}/K_8$. $X_1$ and $K_8$ are again chosen to normnalize parameters.

**SSA model**    The following equations show the dimensionless form of SSA model:

$$\frac{dz_2}{d\tau} = q_1 y_8 z_1 - z_2 \left(q_{-1} + q_2 z_2\right),$$

$$\frac{dz_3}{d\tau} = q_2 z_2^2 - q_3 z_3 z_4 + q_{-3} z_5,$$

$$\frac{dz_5}{d\tau} = q_3 z_3 z_4 - z_5 \left(q_4 + q_{-3}\right) \tag{5.3}$$

$$\frac{dz_6}{d\tau} = q_4 z_5 - q_5 z_6 z_7 + q_{-5} z_8$$

$$\frac{dz_8}{d\tau} = q_5 z_6 z_7 - z_8 \left(q_6 + q_{-5}\right)$$

The assumptions for this system for wild-type cells are

- $z_2(0) = z_3(0) = z_5(0) = z_6(0) = z_8(0) = 0$ and $z_1 = z_4 = z_7 = x_1$ are initial conditions;

- $z_1, z_4$, and $z_7$ are scaled cellular levels of Rad52, ERCC1/XPF, and LigIII enzymes respectively;

- $z_2, z_3, z_5, z_6$, and $z_8$ are scaled intracellular concentrations of many intermediate complexes respectively;

- $q_i$ are scaled rate constants.

- The scaled reaction rates are $q_1 = Q_1 X_1/K_8, q_{-1} = Q_{-1}/K_8, \quad q_2 = Q_2 X_1/K_8, \quad q_3 = Q_3 X_1/K_8, q_{-3} = Q_{-3}/K_8, q_4 = Q_4/K_8, q_5 = Q_5 X_1/K_8, q_{-5} = Q_{-5}/K_8,$ and $q_6 = Q_6/K_8$, again scaled with factors $X_1$ and $K_8$ .

The variables are normalized on Ku total cellular level as $z_i = Z_i/X_1$.

**Alt-NHEJ model**    The Alt-NHEJ intermediate complexes behave as described by the following system of ordinary differential equations:

$$\frac{dw_2}{d\tau} = r_1 w_1 y_6 - w_2 \left(r_2 + r_{-1}\right),$$

$$\frac{dw_4}{d\tau} = r_2 w_2 w_3 - r_3 w_4,$$

$$\frac{dw_5}{d\tau} = r_3 w_4 - r_4 w_5 w_6 + r_{-4} w_7, \tag{5.4}$$

$$\frac{dw_7}{d\tau} = r_4 w_5 w_6 - w_7 \left(r_5 + r_{-4}\right).$$

Where

- $w_2(0) = w_4(0) = w_5(0) = w_7(0) = 0$ and $w_1 = w_3 = w_6 = x_1$;

- $w_1, w_3$, and $w_6$ are scaled cellular levels of PARP1, Pol, and LigI respectively;

- $w_2, w_4, w_5$ and $w_7$ are scaled intracellular concentrations of intermediate complexes;

- $r_i$ are scaled rate constants.

The variables are also normalized per Ku total cellular level as $w_i = W_i/X_1$.
The scaled reaction rates are $r_1 = R_1 X_1/K_8$, $r_{-1} = R_{-1}/K_8$, $r_2 = R_2 X_1/K_8$, $r_3 = R_3/K_8$, $r_4 = R_4 X_1/K_8$, $r_{-4} = R_{-4}/K_8$ and $r_5 = R_5/K_8$.

Table A.1: Values of the involved parameters

| *Parameter* | **Value** | **Parameter** | **Value** |
|---|---|---|---|
| $a$ | 27.5 | $P_{-5}$ | $8.82 \times 10^{-5} h^{-1}$ |
| $b$ | $2.43 \times 10^{-3}$ | $P_6$ | $1.87 \times 10^5 M^{-1} h^{-1}$ |
| $K_1$ | $10.02\ M^{-1} h^{-1}$ | $P_{-6}$ | $1.55 \times 10^{-3} h^{-1}$ |
| $K_{-1}$ | $6.6 \times 10^{-1} h^{-1}$ | $P_7$ | $21.36\ h^{-1}$ |
| $K_2$ | $5.82 \times 10^5 M^{-1} h^{-1}$ | $P_8$ | $1.20 \times 10^4 M^{-1} h^{-1}$ |
| $K_{-2}$ | $5.26 \times 10^{-1} h^{-1}$ | $P_{-8}$ | $2.49 \times 10^{-4} h^{-1}$ |
| $K_3$ | $1.86\ M^{-1} h^{-1}$ | $P_9$ | $4.88 \times 10^{-1} h^{-1}$ |
| $K_4$ | $1.38 \times 10^6 M^{-1} h^{-1}$ | $P_{10}$ | $7.20 \times 10^{-3} h^{-1}$ |
| $K_{-4}$ | $3.86 \times 10^{-1} h^{-1}$ | $P_{11}$ | $6.06 \times 10^{-4} h^{-1}$ |
| $K_5$ | $15.24\ M^{-1} h^{-1}$ | $P_{12}$ | $2.76 \times 10^{-1} h^{-1}$ |
| $K_{-5}$ | $8.28\ h^{-1}$ | $Q_1$ | $7.80 \times 10^3 M^{-1} h^{-1}$ |
| $K_6$ | $18.06\ M^{-1} h^{-1}$ | $Q_{-1}$ | $1.71 \times 10^{-4} h^{-1}$ |
| $K_{-6}$ | $1.33\ h^{-1}$ | $Q_2$ | $3.00 \times 10^4 M^{-1} h^{-1}$ |
| $K_7$ | $2.73 \times 10^5 M^{-1} h^{-1}$ | $Q_3$ | $6.00 \times 10^3 M^{-1} h^{-1}$ |
| $K_{-7}$ | $3.20\ h^{-1}$ | $Q_{-3}$ | $6.06 \times 10^{-4} h^{-1}$ |
| $K_8$ | $5.52 \times 10^{-1} h^{-1}$ | $Q_4$ | $1.66 \times 10^{-6} h^{-1}$ |
| $K_9$ | $1.66 \times 10^{-1} h^{-1}$ | $Q_5$ | $8.40 \times 10^4 M^{-1} h^{-1}$ |
| $K_{10}$ | $1.93 \times 10^{-7}/N_{ir} M$ | $Q_{-5}$ | $4.75 \times 10^{-4} h^{-1}$ |
| $K_{11}$ | $7.50 \times 10^{-2} h^{-1}$ | $Q_6$ | $11.58\ h^{-1}$ |
| $K_{12}$ | $11.10\ h^{-1}$ | $R_1$ | $2.39 \times 10^3 M^{-1} h^{-1}$ |
| $P_1$ | $1.75 \times 10^3 M^{-1} h^{-1}$ | $R_{-1}$ | $12.63\ h^{-1}$ |
| $P_{-1}$ | $1.33 \times 10^{-4} h^{-1}$ | $R_2$ | $4.07 \times 10^4 M^{-1} h^{-1}$ |
| $P_2$ | $7.21\ h^{-1}$ | $R_3$ | $9.82\ h^{-1}$ |
| $P_3$ | $1.37 \times 10^4 M^{-1} h^{-1}$ | $R_4$ | $1.47 \times 10^5 M^{-1} h^{-1}$ |
| $P_{-3}$ | $2.34\ h^{-1}$ | $R_4$ | $12.30\ h^{-1}$ |
| $P_4$ | $5.52 \times 10^{-2} h^{-1}$ | $R_{-4}$ | $2.72\ h^{-1}$ |
| $P_5$ | $1.20 \times 10^5 M^{-1} h^{-1}$ | $R_5$ | $1.65 \times 10^{-1} h^{-1}$ |

# Ringraziamenti

Ho procrastinato per giorni la stesura di queste ultime righe. Non perchè avessi di meglio da fare, ma perchè mi ostinavo a ripetermi che non sarei davvero riuscita a consegnare la tesi. E anche dopo aver avuto la tanto agognata conferma dal mio relatore, il Prof. Marcello Lunardon, ho fissato il titolo di questo ultimo capitolo senza trovare le parole.
Mi ripetevo, notte e giorno: *ce l'ho davvero fatta?*
E intanto mi passavano davanti agli occhi i volti delle persone che in questi due anni hanno colorato le mie giornate.

Pensavo ai miei genitori. Alla Sere che viveva ogni esame con la mia stessa ansia, forse per il mio essere tremendamente drammatica e pessimista (mamma, ricordati che la mela non cade lontano dall'albero). Al Mauri che già sapeva in partenza che ero tragica e non dubitava mai delle mie capacità, ripetendomi che "comunque fosse andata, sarebbe stata una conquista."

Ho visto i volti sorridenti dei miei amici.
C'erano Emma e Vale, che mi sono sempre state vicine, sia a distanza che tra aperitivini e giornate di scottature al mare.
Ho visto anche la Bubba, che tra grattini, l'addormentamento fisso alle 22.00 e i kg di gelato serali, si è dovuta sorbire ogni mio cruccio, ma non ha mai esitato nel darmi un consiglio.
C'erano i miei compagni di corso, che hanno reso lezioni ed esami un po' meno traumatici.
In particolare mi sono soffermanta su Sabrina, che mi ha insegnato che forse l'università non misura quanto si è capaci, e che l'importante è esser felici. E pensare che io in cambio le ho solo piantato in testa quanto fossero necessari i congiuntivi. . .
Poi c'erano le mie compagne di pole.
Chiara, la mia piccola champion, che mi ha insegnato quanto la tenacia possa portare a dei risultati incredibili.
Alice, che con la sua dolcezza mi ha fatto capire che non è così rischioso mostrare le proprie emozioni agli altri.
Nicole, la mia koshi, che non ha mai dubitato un istante delle mie capacità, e che (forse) non mi avrebbe mai lasciata cadere.
Gin, che in un paio di anni è diventata per me un punto fisso, qualcuno su cui contare sempre.
C'era anche Nic che, nonostante tutto, è rimasto parte integrante delle mie giornate e non ha mai smesso di sostenermi. E non ha smesso di torturare Malfy.
Improvvisamente è comparso anche il volto di Alberto, nonchè il mio correlatore e ideatore del lavoro di tesi (alias *capo*), che mi ha sempre spronata a dare il meglio, pronto ad aiutarmi nei momenti di stallo.

Ho pensato anche a Lorenzo, che è comparso verso la fine del mio percorso, scombussolando la mia esistenza dalle radici. In primis perchè mi ha pubblicamente umiliata (leggasi: mi ha battuta a ping pong), e poi perchè ha passato ogni giorno degli ultimi mesi a starmi vicino, rasserenando le giornate più buie. E non mi va di dargli altri crediti, che già se la crede abbastanza.

E man mano che tutti questi volti scorrevano nella mia testa, ho scritto questa specie di ringraziamenti, mentre in me prendeva forma una nuova consapevolezza: *ce l'ho fatta davvero.*

# Bibliography

[1] Valeria Secchi, Angelo Monguzzi, and Irene Villa. "Design Principles of Hybrid Nanomaterials for Radiotherapy Enhanced by Photodynamic Therapy". In: *International Journal of Molecular Sciences* 23 (Aug. 2022), p. 8736. DOI: 10.3390/ijms23158736.

[2] David Azria and Jean-Bernard Dubois. *Item 141 Radiotherapy. Radiobiological notions; main secondary effects; Item 141 Radiotherapie. Notions radiobiologiques; principaux effets secondaires.* Nov. 2006.

[3] Rui-Xue Huang and Ping-Kun Zhou. "DNA damage response signaling pathways and targets for radiotherapy sensitization in cancer". In: *Signal Transduction and Targeted Therapy* 5 (Dec. 2020). DOI: 10.1038/s41392-020-0150-x.

[4] Alethea Wang and Aneil Agrawal. "DNA Repair Pathway Choice Is Influenced by the Health of Drosophila melanogaster". In: *Genetics* 192 (July 2012), pp. 361–70. DOI: 10.1534/genetics.112.143321.

[5] Oleg V. Belov et al. "A quantitative model of the major pathways for radiation-induced DNA double-strand break repair". In: *Journal of Theoretical Biology* 366 (2015), pp. 115–130. ISSN: 0022-5193. DOI: https://doi.org/10.1016/j.jtbi.2014.09.024. URL: https://www.sciencedirect.com/science/article/pii/S0022519314005633.

[6] Wolfgang Schulz. "DNA Damage and DNA Repair". In: Mar. 2023, pp. 51–73. ISBN: 978-3-031-16285-5. DOI: 10.1007/978-3-031-16286-2_3.

[7] J. Valentin. "ICRP Publication 103 – The 2007 Recommendations of the International Commission on Radiological Protection". In: *Annals of the ICRP* 37 (2007).

[8] Hall E.J and Giaccia A.J. *Radiobiology for the Radiologist.* Vol. 7. June 2011. ISBN: 978-1608311934.

[9] D. L. Bailey et al. *Nuclear Medicine Physics.* 2014.

[10] Wesley Bolch et al. "MIRD Pamphlet No. 21: A Generalized Schema for Radiopharmaceutical Dosimetry-Standardization of Nomenclature". In: *Journal of nuclear medicine : official publication, Society of Nuclear Medicine* 50 (Apr. 2009), pp. 477–84. DOI: 10.2967/jnumed.108.056036.

[11] M.Ballan. "Development of targets for the production of radionuclides of medical interest according to the ISOL technique". PhD Thesis. Università degli Studi di Ferrara, 2018.

[12] Michele Ballan et al. "Development of implantation substrates for the collection of radionuclides of medical interest produced via ISOL technique at INFN-LNL". In: *Applied Radiation and Isotopes* 175 (May 2021), p. 109795. DOI: 10.1016/j.apradiso.2021.109795.

[13] Luca Morselli et al. "Production and characterization of 111Ag radioisotope for medical use in a TRIGA Mark II nuclear research reactor". In: *Applied Radiation and Isotopes* 197 (Mar. 2023), p. 110798. DOI: 10.1016/j.apradiso.2023.110798.

[14] O.s Khwairakpam. "Laser photo-ionization study of natAg using opto-galvanic signal at SPES offline laser lab". In: *Journal of Instrumentation* 17 (Dec. 2022). DOI: 10.1088/1748-0221/17/12/C12009.

[15] O.s Khwairakpam et al. "Resonant Laser Ionization and Fine-Structure Study of Silver in an Ablation Plume". In: *Applied Sciences* 13 (Dec. 2022). DOI: 10.3390/app13010309.

[16] Marianna Tosato et al. "Copper Coordination Chemistry of Sulfur Pendant Cyclen Derivatives: An Attempt to Hinder the Reductive-Induced Demetalation in 64/67Cu Radiopharmaceuticals". In: *Inorganic chemistry* XXXX (July 2021). DOI: 10.1021/acs.inorgchem.1c01550.

[17] Roger Alberto et al. "Silver(I) Complexes of the Derivatized Crown Thioether Ligands 3,6,9,12,15,18-Hexathianonadecanol and 3,6,9,13,16,19-Hexathiaicosanol. Determination of Stability Constants

and the Crystal Structures of [Ag(19-aneS6-OH)][CF 3 SO 3 ] and [Ag(20-aneS6-OH)][BF 4 ]". In: *Inorganic chemistry* 35 (June 1996), pp. 3420–3427. DOI: 10.1021/ic951421y.

[18] Marianna Tosato et al. "Toward novel sulphur-containing derivatives of tetraazacyclododecane: synthesis, acid-base properties, spectroscopic characterization, DFT calculations, and Cadmium(II) complex formation in aqueous solution". In: *New Journal of Chemistry* 44 (Apr. 2020). DOI: 10.1039/D0NJ00310G.

[19] Marco Verona et al. "Preliminary Study of a 1,5-Benzodiazepine-Derivative Labelled with Indium-111 for CCK-2 Receptor Targeting". In: *Molecules (Basel, Switzerland)* 26 (Feb. 2021). DOI: 10.3390/molecules26040918.

[20] A. Andrighetto et al. "The ISOLPHARM project: A New ISOL production method of high specific activity beta-emitting radionuclides as radiopharmaceutical precursors". In: *International Journal of Modern Physics: Conference Series* 48 (2018), p. 1860103. DOI: 10.1142/S2010194518601035. eprint: https://doi.org/10.1142/S2010194518601035. URL: https://doi.org/10.1142/S2010194518601035.

[21] *The ISOLPHARM_ADMIRAL Experiment.* URL: https://isolpharm.pd.infn.it.

[22] A. Andrighetto et al. F. Borgna. "preliminary study for the production of high specific activity radionuclides for nuclear medicine obtained with the isotope separation on line technique". In: *Applied Radiation and Isotopes* (2017), pp. 214–226.

[23] *IAEA Human Health Campus.* URL: https://humanhealth.iaea.org/HHW/Radiopharmacy/VirRad/Quality_Control_Procedures/Quality_Control_Module/Radionuclide_Purity/index.html.

[24] L.Morselli. *Production and Characterization of 111Ag for radiopharmaceutical applications in the framework of the ISOLPHARM project.* 2021.

[25] Alberto Arzenton on behalf of the ISOLPHARM Collaboration. "Radiobiological model for $\beta$-emitter radiopharmaceutical therapy in dynamic cell cultures in the framework of the ISOLPHARM project". In: (2023). DOI: 10.1393/ncc/i2023-23072-3.

[26] A.Arzenton. *Monte Carlo based dosimetry using PET/CT and SPECT/CT imaging in radiopharmaceutical therapy in the context of the ISOLPHARM project.* 2021.

[27] A.Leso. *Studio dei radionuclidi prodotti al reattore LENA per il progetto ISOLPHARM EIRA.* Bachelor Degree Thesis. 2021.

[28] S. Incerti et al. "The Geant4-DNA Project". In: *International Journal of Modeling, Simulation, and Scientific Computing* 1.2 (2010). Cited by: 331, pp. 157–178. DOI: 10.1142/S1793962310000122.

[29] Konstantinos P Chatzipapas et al. "Simulation of DNA damage using Geant4-DNA: an overview of the "molecularDNA" example application". In: *Prec.Radiat.Oncol.* (2022), pp. 1–11. DOI: 10.48550/arXiv.2210.01564. URL: https://arxiv.org/abs/2210.01564.

[30] David Edward Charlton, Hooshang Nikjoo, and J. L. Humm. "Calculation of initial yields of single- and double-strand breaks in cell nuclei from electrons, protons and alpha particles." In: *International journal of radiation biology* 56 1 (1989), pp. 1–19. URL: https://api.semanticscholar.org/CorpusID:31521115.

[31] Hooshang Nikjoo et al. "Computational modelling of low energy electron-induced DNA damage by early physical and chemical event". In: *International journal of radiation biology* 71 (June 1997), pp. 467–83. DOI: 10.1080/095530097143798.

[32] Nathanael Lampe et al. "Mechanistic DNA damage simulations in Geant4-DNA part 1: A parameter study in a simplified geometry". In: *Physica Medica* 48 (2018), pp. 135–145. ISSN: 1120-1797. DOI: https://doi.org/10.1016/j.ejmp.2018.02.011. URL: https://www.sciencedirect.com/science/article/pii/S1120179718300346.

[33] WG Shin et al. "A Geant4-DNA Evaluation of Radiation-Induced DNA Damage on a Human Fibroblast". In: *Cancers* 13.19 (2021), p. 4940. DOI: 10.3390/cancers13194940.

[34] Dousatsu Sakata et al. "Evaluation of early radiation DNA damage in a fractal cell nucleus model using Geant4-DNA". In: *Physica Medica* 62 (2019), pp. 152–157. DOI: 10.1016/j.ejmp.2019.04.010. URL: https://www.ncbi.nlm.nih.gov/pubmed/31053372.

[35]   D. I. Filosa. *Ottimizzazione del software per la quantificazione del danno radioindotto al DNA visualizzato attraverso il saggio immunofluorescente γH2AX/53BP1.* Bachelor Degree Thesis. 2020.

[36]   Monika Podhorecka, Andrzej Skladanowski, and Przemyslaw Bozko. "H2AX Phosphorylation: Its Role in DNA Damage Response and Cancer Therapy". In: *Journal of nucleic acids* 2010 (Aug. 2010). DOI: 10.4061/2010/920161.

[37]   Emmy Rogakou et al. "DNA Double-stranded Breaks Induce Histone H2AX Phosphorylation on Serine 139". In: *The Journal of biological chemistry* 273 (Apr. 1998), pp. 5858–68. DOI: 10.1074/jbc.273.10.5858.

[38]   Linda Kuo and Li-Xi Yang. "γ-H2AX- A novel biomaker for DNA double-strand breaks". In: *In vivo (Athens, Greece)* 22 (May 2008), pp. 305–9.

[39]   Emilie Rass, Simon Willaume, and Pascale Bertrand. "53BP1: Keeping It under Control, Even at a Distance from DNA Damage". In: *Genes* 13.12 (2022). ISSN: 2073-4425. DOI: 10.3390/genes13122390. URL: https://www.mdpi.com/2073-4425/13/12/2390.

[40]   Linda Schultz et al. "p53 Binding Protein 1 (53BP1) Is an Early Participant in the Cellular Response to DNA Double-Strand Breaks". In: *The Journal of cell biology* 151 (Dec. 2000), pp. 1381–90. DOI: 10.1083/jcb.151.7.1381.

[41]   Wen-Zhi Tu et al. "gamma H2AX foci formation in the absence of DNA damage: Mitotic H2AX phosphorylation is mediated by the DNA-PKcs/CHK2 pathway". In: *FEBS letters* 587 (Sept. 2013). DOI: 10.1016/j.febslet.2013.08.028.

[42]   Valentina Turinetto and Claudia Giachino. "Multiple facets of histone variant H2AX: A DNA double-strand-break marker with several biological functions". In: *Nucleic acids research* 43 (Feb. 2015). DOI: 10.1093/nar/gkv061.

[43]   Paulina Rybak et al. "Low level phosphorylation of histone H2AX on serine 139 (γH2AX) is not associated with DNA double-strand breaks". In: *Oncotarget* 7 (July 2016). DOI: 10.18632/oncotarget.10411.

[44]   Anyong Xie et al. "Distinct Roles of Chromatin-Associated Proteins MDC1 and 53BP1 in Mammalian Double-Strand Break Repair". In: *Molecular cell* 28 (Jan. 2008), pp. 1045–57. DOI: 10.1016/j.molcel.2007.12.005.

[45]   Stephanie Panier and Simon Boulton. "Double-strand break repair: 53BP1 comes into focus". In: *Nature reviews. Molecular cell biology* 15 (Dec. 2013). DOI: 10.1038/nrm3719.

[46]   Oskar Fdez-Capetillo et al. "DNA damage-induced G(2)-M checkpoint activation by histone H2AX and 53BP1". In: *Nature cell biology* 4 (Jan. 2003), pp. 993–7. DOI: 10.1038/ncb884.

[47]   *Cremona tools.* URL: https://www.cremonatools.it/piastra-di-%20petri-in-vetro-o-60mm.html.

[48]   Radek Machan. "Introduction to Fluorescence Microscopy". In: Jan. 2023. ISBN: 978-3-031-30361-6. DOI: 10.1007/4243_2022_34.

[49]   *Microscope.* URL: https://www.olympus-lifescience.com/en/microscope-resource/primer/techniques/fluorescence/bx51fluorescence/.